

Article

Mass-Transfer and Fluid Flow along Extensional Detachment Faults in Hyperextended Rift Systems: The Examples of Tasna in the Alps, Mauléon in the Pyrenees, and Hobby High Offshore Iberia

Victor Hugo Guimarães Pinto ^{1,*}, Gianreto Manatschal ², Anne Marie Karpoff ², Emmanuel Masini ^{3,4}, Rodolfo Araújo Victor ¹, Adriano Roessler Viana ¹ and Marc Ulrich ²

¹ PETROBRAS S.A, E&P-Exploration, Rio de Janeiro 20231-030, Brazil;

rodolfoavictor@petrobras.com.br (R.A.V.); aviana@petrobras.com.br (A.R.V.)

² CNRS, University of Strasbourg, ITES UMR 7063, 67084 Strasbourg, France; manat@unistra.fr (G.M.); amk@unistra.fr (A.M.K.); mulrich@unistra.fr (M.U.)

³ M&U SASU, 6 Rue de Chamechaude, 38360 Sassenage, France; e.masini@mandu-geology.fr

⁴ ISTerre, University of Grenoble, 38400 Grenoble, France

* Correspondence: vpinto@petrobras.com.br

Abstract: Hyperextended rift systems are characterized by extreme crustal thinning and mantle exhumation associated with extensional detachment faults. These faults cut through thinned continental crust, reaching the underlying mantle and allowing for seawater to infiltrate and react with the crustal and mantle rocks. Hydrothermal fluid systems linked to detachment faults result in fluid–rock reactions occurring along the detachments, resulting in the breakdown and alteration of minerals, loss of elements and strain weakening in both mantle and crustal rocks. We present new geological observations and geochemical data from the modern Iberia and fossil Alpine Tethys Ocean Continent Transition and the West Pyrenean Mauléon hyperextended rift basin. We show evidence for a km-scale fluid flow along detachment faults and discuss the conditions under which fluid flow and mass transfer occurred. Convective fluid systems are of major importance for mass transfer between the mantle, crustal and marine reservoirs. We identified gains in Si, Mg, Fe, Mn, Ca, Ni, Cr and V along extensional detachment faults that we relate to channelized, hydrothermal crust- and mantle-reacted fluid systems migrating along detachments in the hyperextended continental crust. The observation that fault rocks of extensional detachment and syn-extensional sedimentary rocks are enriched in mantle-derived elements such as Cr, Ni and V enables us to define the pathways of fluids, as well as to estimate their age relative to detachment faulting and sedimentation. Because all three examples show a similar mass transport of elements along detachment systems at km-scale, we conclude that these examples are linked to convective fluid systems that may affect the thermal state of the lithosphere, as well as the rheology and chemistry of rocks in hyperextended systems, and may have implications for ore mineral exploration in hyperextended rift systems.

Keywords: rifted margins; fluid flow; detachment faults; mass balance; serpentinization; Alps; Pyrenees; Iberia margin; mantle-reacted fluids



Citation: Pinto, V.H.G.; Manatschal, G.; Karpoff, A.M.; Masini, E.; Victor, R.A.; Viana, A.R.; Ulrich, M. Mass-Transfer and Fluid Flow along Extensional Detachment Faults in Hyperextended Rift Systems: The Examples of Tasna in the Alps, Mauléon in the Pyrenees, and Hobby High Offshore Iberia. *Geosciences* **2023**, *13*, 374. <https://doi.org/10.3390/geosciences13120374>

Academic Editors: Jesus Martinez-Frias, Andrea Brogi, Francisco J. González, A. Filipa A. Marques and Blanca Rincón-Tomás

Received: 19 July 2023

Revised: 18 November 2023

Accepted: 29 November 2023

Published: 8 December 2023



Copyright: © 2023 by the authors. Licensee MDPI, Basel, Switzerland. This article is an open access article distributed under the terms and conditions of the Creative Commons Attribution (CC BY) license (<https://creativecommons.org/licenses/by/4.0/>).

1. Introduction

Fluid-flow and mass transfer not only play an important role in continental metamorphic core complexes [1,2] and oceanic core complexes [3], but also in hyperextended margins [4–6]. While, in metamorphic core complexes, meteoric water interacts with continental crustal rocks, leading to saussuritization and albitization, in oceanic core complexes, the interaction between seawater, mantle and magmatic rocks leads to serpentinization, rodingitization, carbonatization, chloritization, pyritization and other alterations [7] that

are at the origin of white and black smokers [3,8–12]. In contrast, in hyperextended domains and magma-poor Ocean Continent Transitions (OCT), marine fluids interact with both brittle continental crust and subcontinental mantle rocks, distinguishing them from continental and oceanic core complexes. Fluids and minerals related to seafloor weathering and other alteration processes during mantle exhumation have been described at active ultramafic-hosted hydrothermal vents at Mid-Oceanic Ridges (MOR) and OCTs and their chemical composition includes Ca, Mg, Si, Fe and Ni [13–16]. It has also been shown that, when expelled through hydrothermal systems in seawater, the dissolved elements can either precipitate as oxides, sulfides, hydroxides, silicates, or carbonates, or alternatively be absorbed in sediments [15–19].

The role of fluid flow at hyperextended rifts and magma-poor rifted margins, where seawater can interact with continental crustal and mantle rocks along extensional detachment systems, is much less understood [4,20,21]. In these settings, serpentinization is a common process [22] and can extend down to 5–6 km below the seafloor, as indicated by seismic refraction data from the Iberia and Newfoundland margins (Figure 1a) [23,24]. Pinto et al. [25] showed that serpentinization of the subcontinental mantle initiates prior to its exhumation at the seafloor underneath a thin, <6 km thick continental crust and involves a considerable volume of fluids enriched in elements derived from the hydrating continental crust and underlying mantle. These fluids migrate along extensional detachment systems into the supra-detachment basins, leaving geochemical fingerprints, as indicated by the relative enrichment of Ni, Cr and V compared to the average composition of the surrounding continental crust [4]. Pinto et al. [25] showed that hydrothermal systems related to hyperextension and mantle exhumation may also have a strong impact on seawater composition, marine biosphere, the nature of sediments and diagenetic processes. In contrast to MORs that are also linked to important mass transfer but operate in open and connected oceans [13,17], during hyperextension, seaways are not yet connected, resulting in higher element concentrations in seawater of the often-restricted rift basins. However, at present, only a few systematic studies from hyperextended rift examples exist, one from the Err detachment system in SE Switzerland [4] and a few from the Pyrenean and Basque-Cantabrian Basins [6,21,26] (Figure 1b). These detachment systems are formed during hyperextension of a less than 10 km thin crust, simultaneously with mantle exhumation.

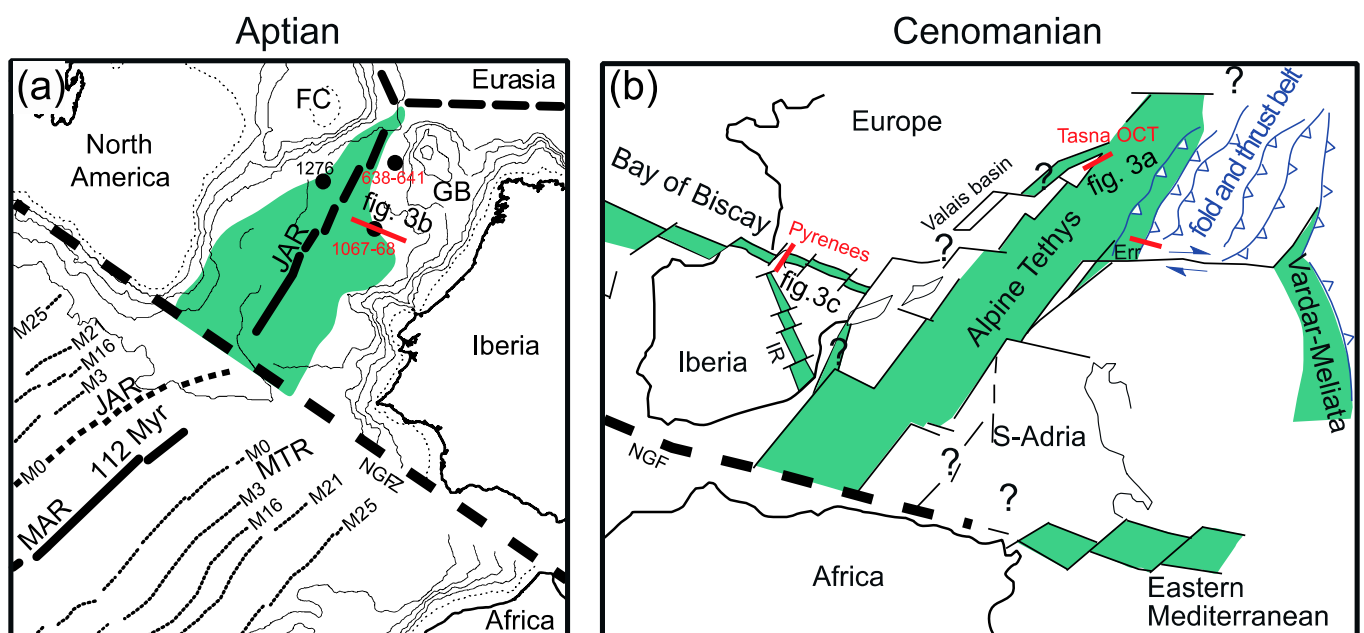


Figure 1. Paleogeographic maps showing the locations of the studied examples at the moment of breakup, when basins were not fully connected to the global oceans. Green polygons mark hyperextended domains

where the mantle was exhumed at the seafloor. (a) Paleogeographic map of Newfoundland–Iberia at Aptian time. FC: Flemish Cap, GB: Galicia Bank, JAR: J-Anomaly Ridge; NGFZ: Newfoundland–Gibraltar Fracture Zone (NGFZ). Dots mark the ODP Sites and a red line marks the seismic section used in this work. Map modified from Tucholke and Sibuet [27]. (b) Paleogeographic map of the Alpine Tethys and the Pyrenean domain between Iberia and Europe. The red lines are the sections from Mauléon Basin and Tasna OCT. IR: Iberia Internal Range. See also the location of the Err detachment system at the distal Adriatic margin. Map modified from Manatschal and Müntener [28].

The aim of this study is to investigate other hyperextended systems and to test if element losses due to alterations in continental crust (e.g., saussuritization) and mantle rocks (e.g., serpentinization) can be detected in the sedimentary rocks and fault rocks of detachment faults within the hyperextended continental crust related to mantle exhumation. We also will elucidate the systematics of mass transfer to understand the link between saussuritization, serpentinization, hydrothermal activity and extensional systems by testing if a geochemical signature of these processes can be found in fault rocks within the hyperextended continental crust and the overlying syn-exhumation sedimentary rocks.

2. Examples of Detachment Faults and Related Fluid Flow in Hyperextended Rift Systems

Hyperextended rift systems are characterized by a thinned embrittled continental crust (less than 10 km thick) transected by extensional detachment fault systems [29,30]. The transition from thinned continental crust to exhumed mantle, and then to oceanic crust, commonly referred to as an OCT, is well-documented at the Iberia–Newfoundland conjugate margins (Figure 1a) [31,32] (and references therein) and in the Alps (e.g., Tasna OCT; Figure 1b) [33,34]. The examples studied here reached different maturities in their rift evolution. While the Iberia–Newfoundland system attained steady-state seafloor spreading, an unequivocal oceanic crust is not documented in the Alpine Tethys example [35]. At the Mauléon basin in the Western Pyrenees, rifting failed before the onset of seafloor spreading [36,37]. Despite the different models that were proposed to explain the studied sites, they share similar characteristics, such as the strong hydration of the crust and mantle during hyperextension and mantle exhumation, the exhumation of mantle preceding the first emplacement of basalts at the seafloor and rift-related magmatic rocks that are absent over the hyperextended continental crust (Figure 2). These observations are generally accepted and form the foundation of our study.

A geological model was proposed to explain the formation and migration of crustal- and mantle-reacted fluids in a hyperextended rift system based on the example of the Err detachment in the Alps ([4]; Figure 2). In this system, faults cut through the thinned, <10 km thick hyperextended continental crust into the mantle (Figure 2b) and serve as pathways for the downward migration of seawater into the actively deforming and, therefore, permeable subcontinental mantle. Although the exact downward pathways of the fluids responsible for the initial serpentinization of the mantle remain to be defined, Hochscheid et al. [38] demonstrated, using the example of the Tasna OCT and Sr isotopes, that the fluids are marine-derived and move through the thinned, <10 km thick crust before reaching the underlying mantle. The progressive mantle exhumation along active detachment systems in the hyperextended domains results in dynamic permeability, which favors the creation of convection cells responsible for the serpentinization of the mantle during exhumation (Figure 2c). All these processes result in the leaching of elements from the mantle reservoir and the formation of mantle-reacted fluids with a well-defined chemical signature (e.g., Ni, Cr, V). The possible magmatic origin of these elements can be excluded, since all three studied sites did not show evidence of magma extrusion during exhumation. The mantle-reacted fluids migrate upward along active extensional detachment faults, through a thinned continental crust, towards the seafloor, where they can either react with sediments or mix with seawater (Figure 2d–e). It is important to highlight that fluid flow and rocks in hyperextended systems are different from those observed at MORs. However, in contrast

to MORs, hyperextended and OCT systems have only been tested, to date, in one example, which is the Err detachment in the Swiss Alps [4]. This study aims to validate and improve this model and to demonstrate that hyperextension is linked to large-scale and intense fluid and mass transfer.

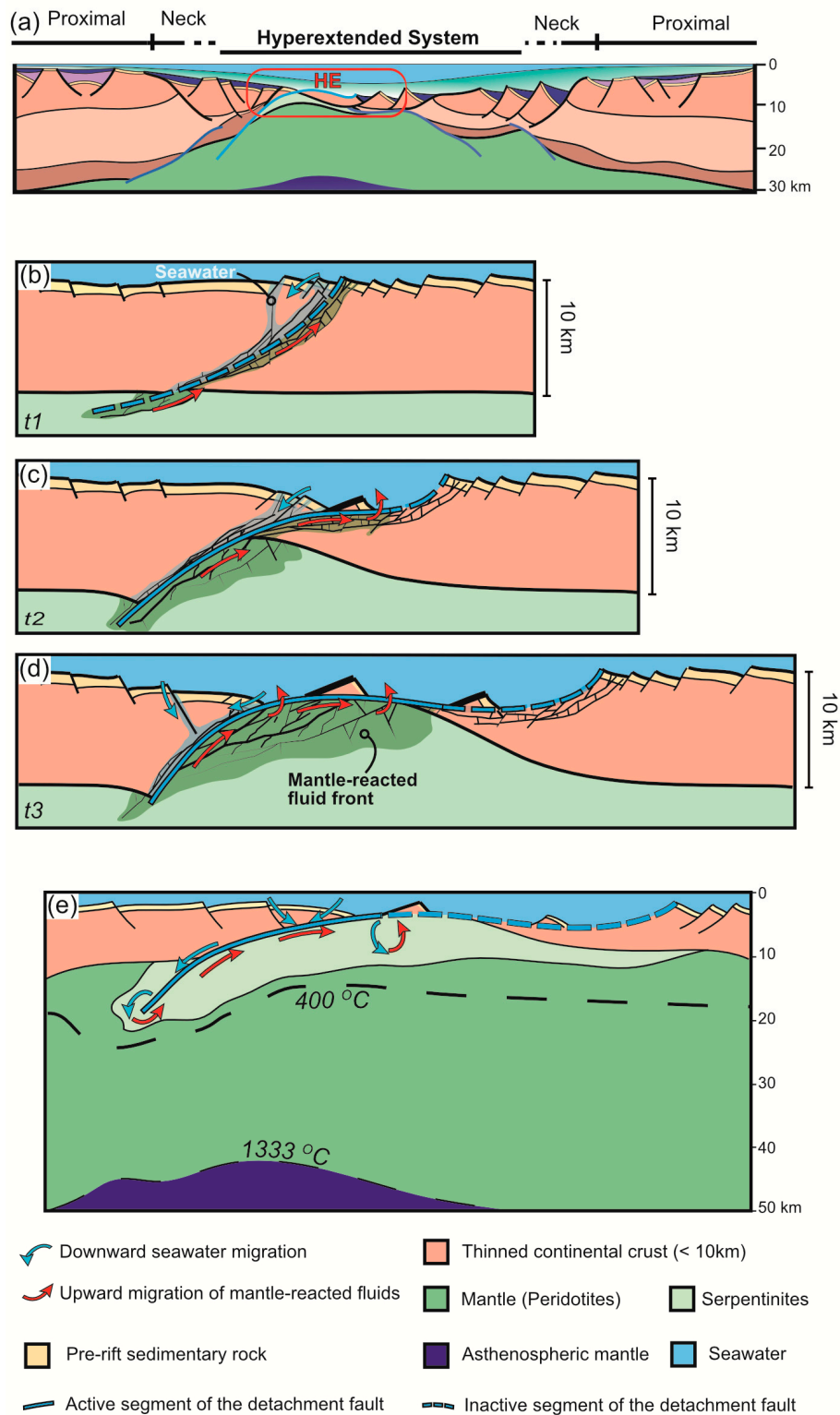


Figure 2. Relationship between the evolution of a hyperextended system and fluid flow. (a) Location of the hyperextended system (HE). Red square marks HE and fluid evolution shown from (b–e). Note

that the time steps of the evolution of the detachment fault system and fluid flow are indicated by t_1 – t_3 . (b) The fault system cuts through the already thinned continental crust into the mantle, triggering serpentinization. (c) Mantle exhumation along active detachment systems. Deformation of the continental crust, together with fluid flow, also results in its alteration (saussuritization). (d,e) Mantle exhumation and simultaneous serpentinization. Fluids migrate upward along active extensional detachment faults towards the seafloor, where they can either react with sediments or pollute seawater. (e) Schematic lithosphere at the time of mantle exhumation. Subfigures (b–e), modified from [4].

The three hyperextended systems presented in this study (Figure 1) are among a handful of examples worldwide from which rock samples are accessible and can be analyzed. These rock samples provide a unique opportunity to characterize the link between the role of fluids during hyperextension and mantle exhumation in OCTs.

2.1. The Tasna OCT in the Alps

The Tasna OCT exposed in the Swiss Alps is a unique field example preserving the primary structure of an OCT. The exposed outcrop is 6 km wide and preserves 600 m of the vertical section [34,39,40] (Figure 3a). The top of the continental basement is characterized by the extensional Upper Tasna Detachment (UTD), which is composed of cataclasites and gouges overlain by tectono-sedimentary breccias and sealed by Upper Jurassic to Lower Cretaceous post-rift sedimentary rocks. The tectono-sedimentary breccias are rocks overlaying the fault rocks form the basal sequence of supradetachment basins [41] (and references therein). They show characteristics of sedimentary deposition with minimum transport and some indication of tectonic deformation. In the Tasna OCT, those rocks are silica-cemented and composed of clasts of granite, gneiss and migmatites derived from the reworked underlying exhumed footwall. The continental basement is floored by a second extensional detachment fault, the Lower Tasna Detachment (LTD), which consists of serpentinite cataclasites, some of which are foliated [40]. Rift-related magmatic rocks do not occur in the Upper Tasna unit investigated here.

$^{40}\text{Ar}/^{39}\text{Ar}$ on phlogopites from pyroxenites within the mantle led to results of 169.1 ± 0.4 and 170.5 ± 0.4 Ma [40] and have been interpreted to date the exhumation of the mantle through ~ 350 °C in the footwall of the LTD. This temperature is within the serpentinization window [42] and corresponds to a depth of ≤ 6 km, assuming normal thermal gradients in hyperextended domains. U-Pb dating on zircons derived from small veins of K-rich and Ca-poor alkaline magmatic rocks exposed south of the Engadine valley within the same tectonic unit were 167.3 ± 2.7 Ma, interpreted as crystallization ages. $^{40}\text{Ar}/^{39}\text{Ar}$ dating on phlogopite from the same samples were 167.55 ± 0.9 and 167.9 ± 1.4 Ma, interpreted as cooling ages [34,43]. Therefore, the age of serpentinization, incipient magmatism and subsequent mantle exhumation are interpreted to be late Middle Jurassic, similar to ages obtained for mantle exhumation and initial magmatism all along the Alpine Tethys margins [44].

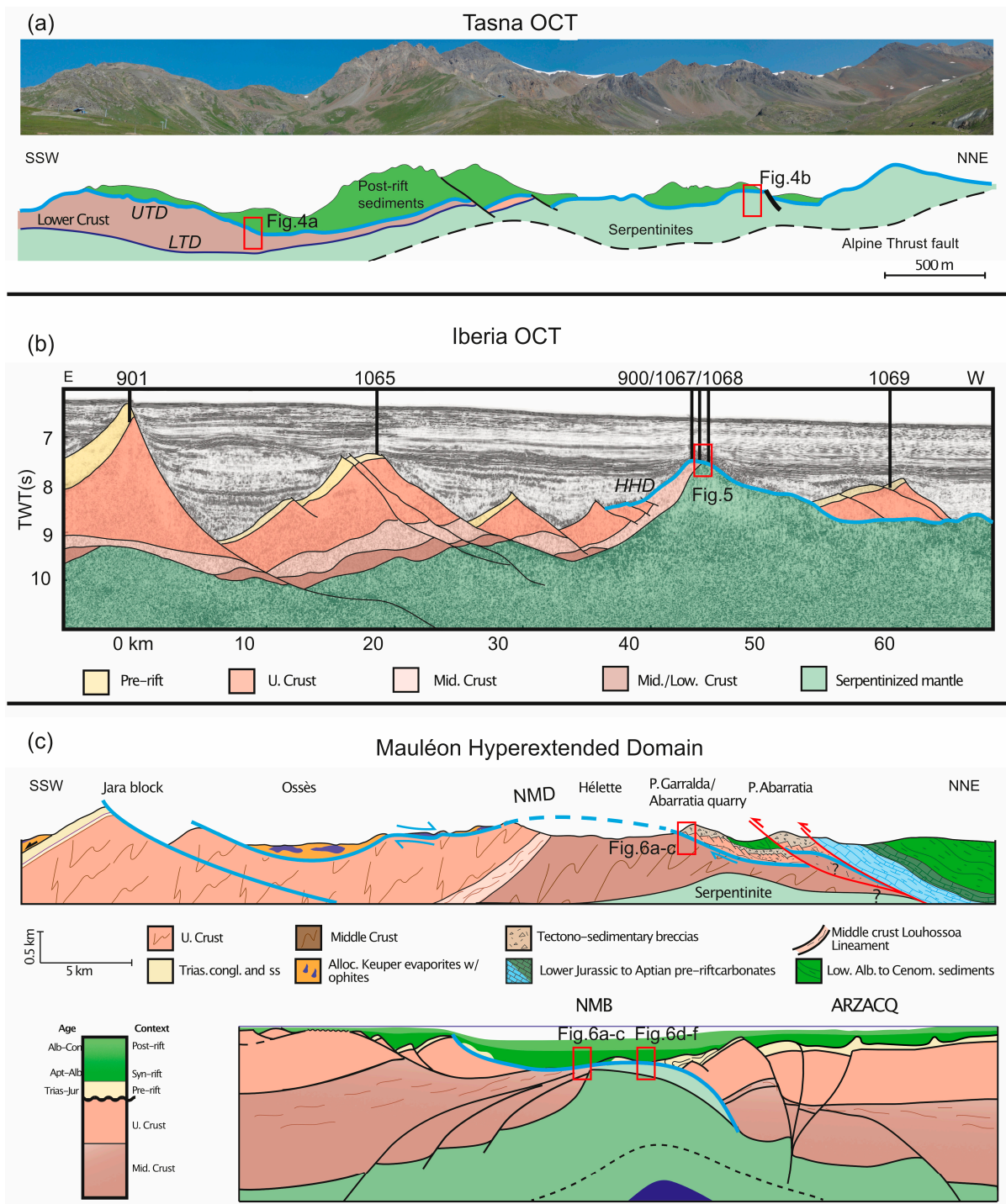


Figure 3. Hyperextended domains. (a) Photo of Tasna OCT at the top and its interpretation below. UTD: Upper Tasna Detachment; LTD: Lower Tasna Detachment. After [39,40]. The location of Tasna outcrop is 46.82° N/ 10.25° E. (b) Reflection seismic section Lusigal-12 at the Iberia margin. HHD: Hobby High Detachment (location at 40.6° N/ 11.6° W). The numbers at the top are the ODP Sites. (c) Geological section at the top, from the breakaway fault (Jara) to the most distal segment of the North Mauléon Detachment (NMD). The red lines are thrust faults formed during Pyrenean convergence. Although the serpentinites do not outcrop at the surface in this section, a mantle outcrop occurs a few kilometers further west. The section below shows the reconstruction of the hyperextended system (modified from Masini et al. [35]). Location: Jara block (43.19° N/ 1.29° W) and Pic de Garralda (43.34° N/ 1.24° W).

2.2. The Hobby High Offshore Western Iberia

The Hobby High (Figure 3b) is located at the oceanward termination of the hyperextended continental crust at the Western Iberia Margin. It corresponds to the first exhumation of subcontinental mantle along an extensional detachment fault that was drilled at ODP Sites 900, 1067 and 1068 [29,45–47].

The hyperextended domain of the Iberia Margin comprises a thinned continental crust and exhumed subcontinental mantle overlain by an extensional allochthon of continental crust (e.g., ODP Site 1069; [47]). Mafic extrusive rocks have not been drilled. The exhumed mantle domain extends up to 200 km oceanward [29].

The age of mantle exhumation and OCT formation was constrained by dating the overlying sedimentary rocks using radiometric methods. Microfossils in the matrix of the ultramafic-bearing debris deposited over the exhumed mantle are dated as ranging from Valanginian to Barremian; however, the Valanginian microfossils are thought to be reworked [48], but provide a maximum age for exhumation. The emplacement of gabbros further oceanwards in the previously serpentinized mantle from ODP Site 1070 was dated using U-Pb on zircons as 127 ± 4 Ma [49]. Younger alkaline magmatic veins dated by U/Pb on zircons show ages of 113 ± 2 Ma [49]. Therefore, the ages of the mantle exhumation, the incipient magmatism and the formation of the >150 km wide OCT are considered to occur between Barremian and the latest Aptian, corresponding to a time interval of approximately 18 myr, which corresponds to exhumation rates of about 1 mm/yr.

2.3. The Mauléon Basin in the Western Pyrenees

The Mauléon Basin in the Western Pyrenees preserves remnants of a hyperextended system, showing evidence of incipient mantle exhumation (Figure 3c) [50]. Mantle exhumation is evidenced by small outcrops of serpentinites, less than 1.1 km², occurring several places along the axis of the hyperextended basin, and by the reworking of mantle rocks in Cretaceous sedimentary rocks [21,50–53]. An extensional detachment fault, the North Mauléon Detachment (NMD), is associated with upper and mid-crustal rocks and has been interpreted to be responsible for the exhumation of the subcontinental mantle in the Mauléon basin [35,50,54]. ⁴⁰Ar/³⁹Ar on phlogopite from a gabbroic dike intruded in mantle rocks provided ages between 108 and 105 Ma, interpreted as cooling ages [35]. Hart et al. [55] constrained the age of exhumation to Albian time and showed that exhumation occurred at elevated thermal gradients of from 80 to 100 °C/km. The exhumed mantle is sealed by Albo-Cenomanian sedimentary rocks, providing a minimum age for the exhumation. Therefore, the hyperextension and incipient mantle exhumation in the Pyrenees are interpreted to occur between 108 and 94 Ma, which provides a time interval of 14 myr. The early exhumation discussed here was not directly associated with the emplacement of mafic extrusive rocks.

3. Field, Petrological and Structural Observations

3.1. Crustal Basement Rocks in the Hyperextended Domains

The continental basement rocks forming the hyperextended domains are different at the three studied sites. In the Tasna OCT, the basement is made of gneisses, migmatites and mylonitized and strongly hydrated meta-gabbros, derived from the pre-rift middle to lower crust [34].

At Hobby High, the continental basement drilled at ODP Sites 1067 and 900 is characterized by amphibolites, meta-gabbros and tonalites that represent the pre-rift middle to lower crust [56]. The tonalite gneisses consist of coarse plagioclase and amphiboles with lenses of anorthosite that sometimes show sharp and diffuse contacts with the amphibolites [46,47]. Diffuse contacts suggest that anorthosites spread throughout the basement, indicating that plagioclase is an important component of the basement constituting the Hobby High. Calcite, epidote and chlorite veins are common in the basement rocks and may be directly linked to their penetrative alteration and hydration.

The basement rocks associated with the North Mauléon Detachment (NMD) in the Western Pyrenees are composed of two main groups: (1) upper crustal meta-sediments, which are mainly Ordovician and Silurian quartzites and schists, and (2) mid-crustal rocks assumed to be pre-Cambrian in age and corresponding to para-gneisses in their amphibolite and granulite facies [57]. These two groups of rocks are separated by the W–E striking Louhossoa lineament that may correspond, according to the obtained ages of its footwall, to a rift-related structure separating upper- from mid-crustal rocks truncated by the NMD [35,50].

It is important to note that all rocks investigated in this study derive from the hyperextended continental crust and are associated with the detachment systems that form during hyperextension and root in the underlying subcontinental mantle. Mafic extrusive rocks do not occur in the vicinity of the studied sites and did not form during the exhumation stage investigated in this study.

3.2. Fault Rocks in the Continental Basement

The fault rocks from all studied areas are characterized by brittle structures that exhibit a gradual increase in deformation towards the top of the continental basement. In the Tasna OCT (Figure 4a), the UTD is made of up to 100 m of cataclasites transected by anastomosing gouge layers, which range from centimetric to metric in thickness. The gouges become more common upsection (Figure 4(a1)). Syn- to post-tectonic quartz and calcite veins are common in the fault zone and, in most cases, quartz veins crosscut the calcite veins, but the opposite can be observed as well [19]. A cataclastic foliation overprints an older gneissic fabric and becomes stronger towards the top of the basement, which corresponds to the core zone of the extensional detachment fault. Foliated cataclasites (Figure 4(a2)) result from progressive brittle deformation and saussuritization. The saussuritization is responsible for the: (i) breakdown of feldspars due to albitization, (ii) chloritization of plagioclases and biotites (rarely observed), and (iii) alterations in feldspar to sericite and illite. Microstructural analysis shows that the gouges are characterized by a well-developed foliation, defined by a chlorite–illite–sericite-rich matrix, rounded clasts of quartz veins and cemented cataclasites. In both cataclasites and gouges Fe-oxides are frequent in syn-tectonic foliation. SEM analyses show that the breakdown of plagioclase is often accompanied by quartz and calcite veins. Fe-rich chlorite veins cut and react with plagioclase, leading to the formation of chamosite (Figure 4(a4)).

At Hobby High (Figure 5a(a2)), the drilled damage zone is up to 50 m thick. The HHD is made of cataclasites and gouges that grade upsection into fault breccias (ODP Site 1067) [47]. Cataclasites are characterized by clasts surrounded by a chlorite-rich matrix transected by veins of chlorite, epidote and rarely calcite. Foliated cataclasites are locally observed and exhibit from millimetric to centimetric clasts of amphibolite and quartzo-feldspathic rocks in a foliated matrix composed of chlorite, epidote and calcite. Gouges are strongly foliated, and the matrix contains chlorite and recrystallized micro-sparite. Fault breccias usually contain clasts of amphibolite up to 20 cm in diameter and tend to change from clast- to matrix-supported further up the section. Fe-oxyhydroxide banding is often observed in the matrix of these fault rocks. Late-stage calcite veins (up to 2 mm) usually cut the epidote and chlorite veins.

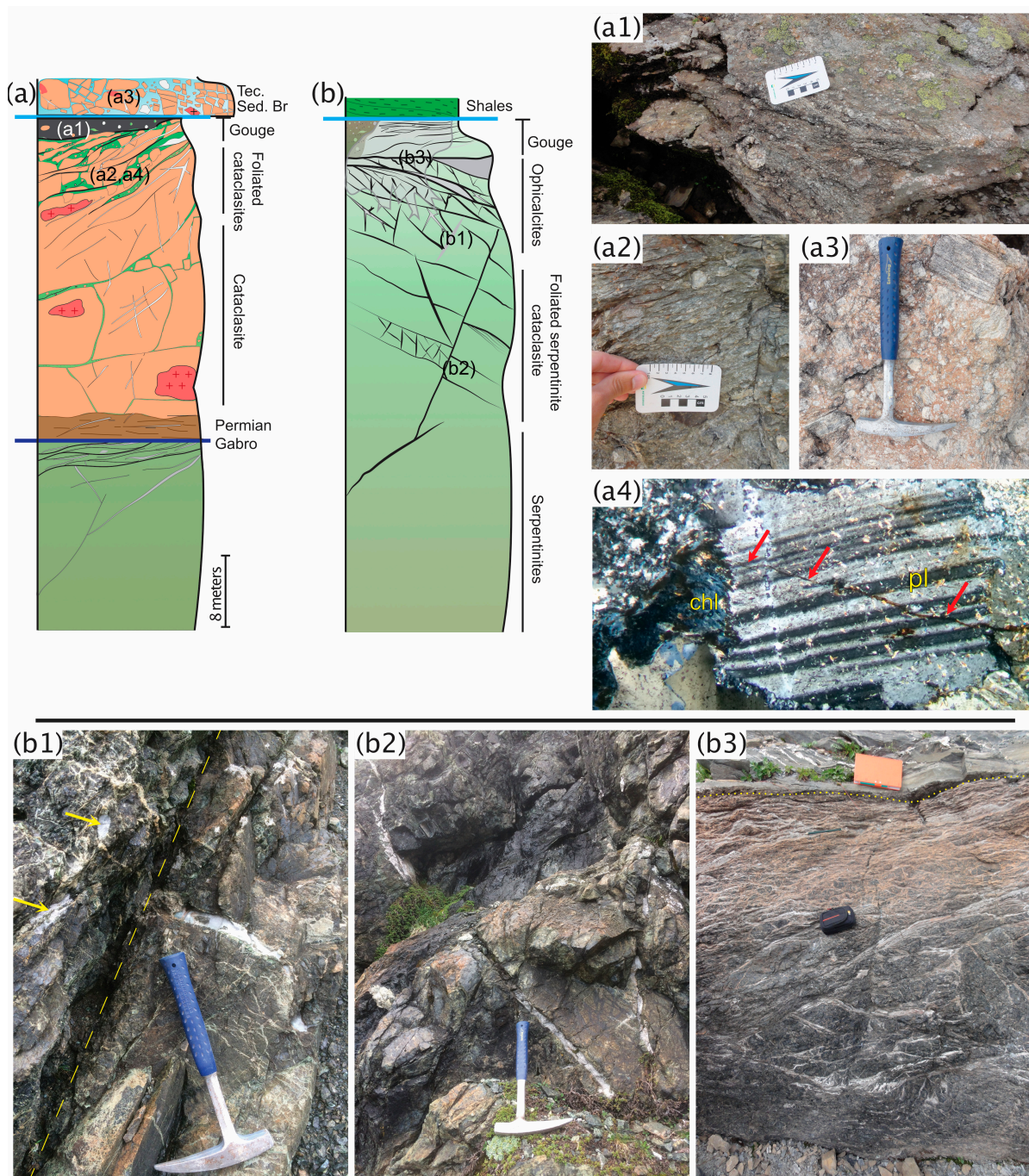


Figure 4. Fault rocks from the Upper and Lower Tasna detachment. **(a)** Section across the UTD (light blue line) and LTD (dark blue line) through the continental wedge (south). **(b)** Section across the UTD in the exhumed mantle (north). Photos **(a1–a4)** show the fault rocks in the continental crust and **(b1–b3)** in the mantle. **(a1)** Gouge layer at the top of the UTD. **(a2)** Foliated cataclasite with centimeter-thick lenses of gouges. **(a3)** Tectono-sedimentary breccia with silicified matrix. **(a4)** Chlorite forming at the plagioclase rim in the cataclasite. Note a small iron-bearing vein (red arrow) cutting the plagioclase(pl) and connecting the chlorite(chl); see explanation in the text. **(b1)** Foliated cataclasite and calcite veins (yellow arrows) in the mantle of the LTD. Elongated clasts of calcite in the foliation show that some calcite veins are syn-kinematic. The brittle fault zone made of foliated cataclasite truncates an older foliation and calcite vein (below the yellow dashed line). **(b2)** Large calcite veins cutting the serpentinites in the LTD. **(b3)** Increase in strain from bottom to top of the UTD, evidenced by a more penetrative foliation between the field book and the camera case. Shales overlying the top of the mantle along UTD (yellow dash line).

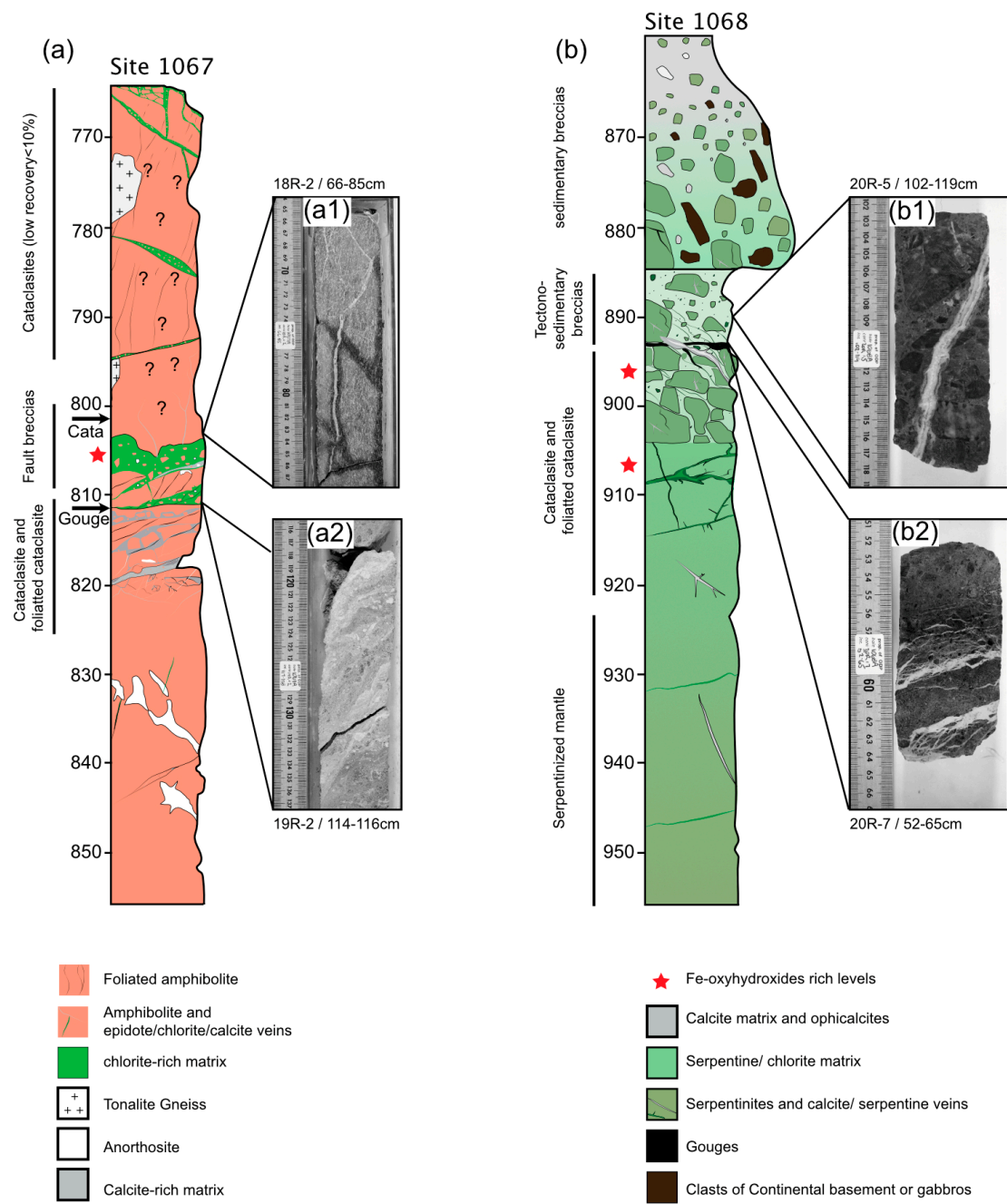


Figure 5. Fault rocks from the Hobby High Detachment (HHD). The descriptions on the left side of the profiles represent the predominance of lithotypes, but are not restricted to them. (a) The fault zone’s profile at ODP Site 1067. Black arrows show the location of samples used for mass balance. (a1) Calcite veins crosscutting the weakly brecciated amphibolite. (a2) Cataclasite at the base of the dipping normal fault and gouge with a calcite-rich matrix (whitish area). (b) Fault zone profile across the exhumed mantle drilled at ODP Site 1068. (b1) Tectono-sedimentary breccia cut by calcite vein. (b2) Fault breccia with transposed calcite veins.

The damage zone of the NMD in the Mauléon basin is up to 30 m thick and composed of dark red cataclasites and foliated cataclasites and rare gouges (Figure 6a–c). The NMD formed in upper-crustal, low-grade Devonian–Ordovician quartzites and schists near the fault’s breakaway (Jara and Ossès sites; see Figure 3c for location and [35]) and penetrated in a granulitic basement (Pic de Garralda/Abarratia quarry, see Figure 3c). Structural and microstructural analyses of the granulitic rocks show that the foliated cataclasites are made

of clasts of quartz, sericitized feldspars and rounded agglomerates of quartz. The foliated cataclasites are composed of syn-tectonic curve-shaped sericite/illite and chlorite (minor), as well as Fe-oxyhydroxides, which are responsible for their dark red color (e.g., outcrop Pic de Garralda; Figures 3c and 6b). The NMD is overprinted by a series of sub-vertical normal faults, which also characterize the damage zone of the NMD, as documented in the Abarratia quarry (Figure 6c). Where the cataclasites developed from Devonian–Ordovician quartzites and schists, feldspar minerals are strongly sericitized and Fe-oxides and the dark pink matrix of Mn-oxides are frequently observed in centimetric cataclastic layers. Along the NMD, high concentrations of Fe-oxides can be found in the foliated matrix of the cataclasites. These oxides occur all along the NMD from the fault's breakaway at Jara (see Figure 3c), where Fe-oxides are also observed in the Triassic pre-rift sedimentary rocks to the Pic de Garralda in the north.

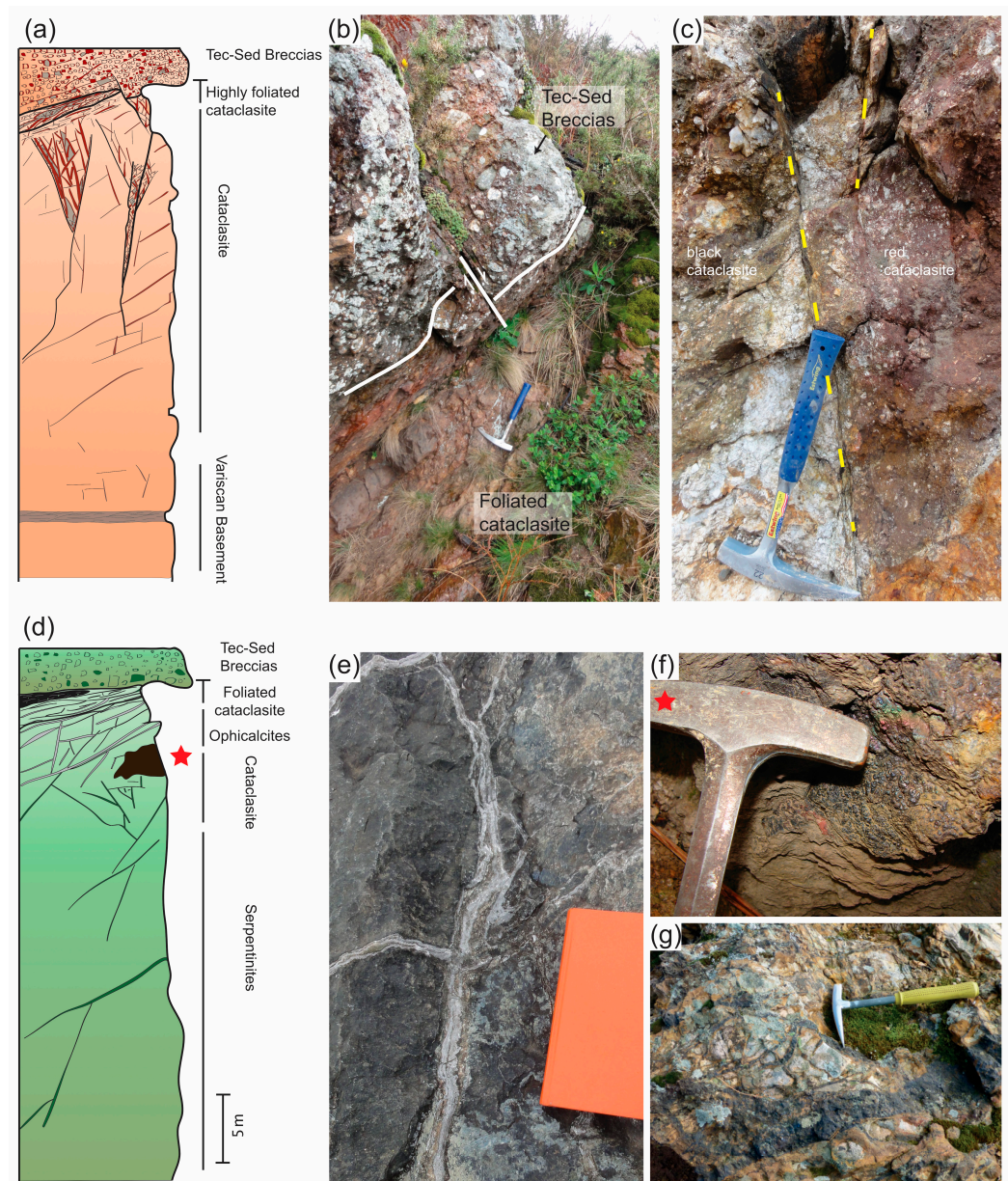


Figure 6. Sections across the fault zone of the North Mauléon Detachment (NMD) and the exhumed mantle. (a) Fault zone profile across the NMD. (b) Outcrop at the Pic de Garralda showing the low-angle contact (015/45) between foliated cataclasites and tectono-sedimentary breccias. (c) The fault

zone is made of cataclasites cut by secondary sub-vertical normal faults (dashed lines) at the Abarriatia query (see Figure 3c for location). The reddish color in previous photos highlights the presence of Fe-oxides. (d) Fault zone profile across the top of the exhumed mantle. Note the Fe-oxide layer at the serpentinites (red star). (e) Calcite veins cut the serpentinites. (f) Fe-oxides crust formed in the serpentinites. See the red star for location in (d). (g) Veins of Fe-oxyhydroxides in the Triassic sedimentary rocks from the breakaway of NMD.

3.3. The Serpentinized Mantle Rocks

The mantle exposed at all three studied sites is made of serpentinized lherzolites and pyroxenites, as well as of harzburgites and dunites. Thus, the overall composition of the mantle in OCTs is different from that of MORs and is, in general, much more enriched. The main serpentine polymorphs observed in the exhumed mantle rocks along the OCTs are chrysotile and lizardite [58,59]. Oxygen isotopes on chrysotile/lizardite from the Alps, Pyrenees and Iberia point to temperatures higher than 175 °C for early stages of serpentinization and a temperature between 25 and 100 °C for the final stages of serpentinization and seafloor weathering during and after mantle exhumation at the seafloor (for methods and data, see [59–64]. Oxygen isotope analyses of calcite veins and the carbonate matrix of ophicalcites point to a broad range of temperature conditions suitable for their formation (for data and methods, see [16,59,62,63,65]).

The mantle exposed in the Tasna OCT is composed of serpentinized spinel-lherzolite and pyroxenite layers [40]. The serpentinized peridotite often exhibits a well-developed, high-temperature spinel foliation at the bottom of the section. Although the mantle rocks are more than 90% serpentinized, original igneous textures are locally preserved. Olivine is replaced by chrysotile/lizardite, spinel is rimmed by magnetite, and pyroxene is commonly serpentinized or chloritized. Ti-hornblende and phlogopite are locally preserved in pyroxenite layers. Further up the section, olivine and pyroxene are completely altered to serpentine. The foliation is usually cut by multi-stage veins of chrysotile/lizardite, and is also locally cut by calcite veins.

At the Iberia margin, the serpentinite mesh structures contain submicroscopic fibers of lizardite and brucite. Beard and Hopkinson [66] highlighted the occurrence of andradite and hydroandradite (garnet group Ca-Fe-silicate and hydrated silicate) in the matrix, which are intergrowing with serpentine minerals. Serpentine veins are common in these rocks and are often accompanied by Fe-Ni alloys and Ni-sulfides. Calcite veins containing Fe, Mn and Mg in the form of oxyhydroxides and carbonate, were described at ODP Sites 897 and 899 [61]. They are a common feature in the upper part of the exhumed mantle and usually cut older lizardite/chrysotile veins [67].

In the Western Pyrenees (e.g., Col d'Urdach) the mantle is characterized by serpentinized lherzolite and minor harzburgite, with up to 80% serpentinization [50,53]. In the thin section, serpentine replaces olivine and relicts of pyroxenes, rimmed by serpentine and chlorite, are locally preserved. Chrysotile/lizardite veins usually cut the rock in several directions and Fe-oxides usually occur within the veins. Large concentrations of Fe-oxides, up to 0.5 m wide, occur in the serpentinites (e.g., Col d'Urdach). In thin sections, intergrowth contacts are observed between quartz and Fe-oxides as well as Fe-oxide veins. Ophicalcites are common [64,65] and can be cut by centimeter-thick grayish calcite veins that may be related to crack-seal processes. In thin sections, these veins often display syntaxial and asymmetric growth and they are accompanied by micrometric Fe-oxide patches. Brownish micritic and sparry calcites grew over the serpentine and the previously described calcite veins are the latest mineral phases formed in these rocks.

3.4. Fault Rocks in the Mantle

The fault zones in the serpentinized mantle in all three sites share many similarities regarding protolith, types of fault rocks, veins and geochemical composition. The fault rocks are characterized by cataclasites, foliated cataclasites, fault breccias and gouges. They formed under lower greenschist facies conditions in the brittle field, as evidenced by

neo-formed, low-temperature minerals (e.g., chrysotile, lizardite and chlorite) defining the foliation in the fault rocks. The lack of evidence for crystal plastic deformation in the fault rocks suggests that the extensional detachment faults may have been rooted at shallow levels (<12 km).

At the Iberia margin, fault rocks in the exhumed mantle were sampled by drilling at ODP Sites 1068, 1070, 897 and 899 [45,46]. The thickness of the fault zone exceeds 50 m, as indicated by drilled wells that did not penetrate undeformed serpentinites (e.g., Site 1068). From bottom to top, the fault rocks are made of cataclasites, foliated cataclasites, fault breccias and gouges (Figure 5b(b2)). Cataclasites show typical jigsaw clasts within a “matrix” made of chrysotile/lizardite. Foliated cataclasites are characterized by a chlorite- and serpentine-rich matrix, which is sometimes also rich in calcite. Fault breccias tend to change from clast- to matrix-supported up-section. They are composed of millimeter-to-centimeter clasts of serpentinites and local pyroxenites. Their matrix is made of chlorite, serpentine, Fe-oxyhydroxides and usually pervasive sparitic calcite. Fault breccias are heavily cut by calcite veins and exhibit local jigsaw clasts. The clasts of some fault breccias tend to “float” in the calcite matrix, suggesting that they are formed by the influence of high-pressure fluids (e.g., Section 1070A-8R-1). In these zones, quartz veins are sometimes filling fractures (e.g., Section 1070A-8R-3). Gouge layers are characterized by rounded clasts, as well as by serpentine and calcite veins that are sub-parallel to the tectonic foliation. These gouges are commonly transected by younger calcite veins. All the aforementioned veins present the same characteristics as previously described for the serpentinites. Up-section, tectono-sedimentary breccias and matrix-supported sedimentary breccias overlie the top of the fault zone (Figure 5b).

At the Tasna OCT [40], the mantle fault rocks along the UTD (Figure 4b(b3)) are characterized from bottom to top by: (i) cataclasites showing jigsaw clasts and fractures filled by serpentine veins, (ii) foliated cataclasites with centimetric to decimetric angular clasts of serpentinites cut by chrysotile/lizardite/chlorite veins, (iii) matrix-supported tectonic breccias heavily cut by serpentine/chlorite/calcite veins, and (iv) local millimetric to centimetric gouge layers with chlorite/serpentine matrix and millimetric rounded clasts. Serpentine veins are always present in the fault zone, and they are commonly cut by Fe-oxide-bearing calcite veins. The frequency of calcite veins increases from bottom to top across the UTD fault zone. The types of fault rocks observed along the LTD (Figure 4(b1,b2)) are quite similar to those described from the UTD, with two main exceptions. First is the occurrence of layers composed of chlorite and serpentine that show a strong foliation, which is locally observed close to the contact with the altered meta-gabbros belonging to the continental crust. The second is the relationship between serpentine and calcite veins in the cataclastic foliation. The calcite veins are cut by a brittle fault zone and clasts of calcite can be found in the foliation of this structure (Figure 4(b1)).

The fault zone in the exhumed mantle in the Mauléon Basin is only locally exposed (Figure 6d). However, cataclasites like those found along the Tasna OCT are observed. They are crosscut by late, millimetric to centimetric calcite veins (Figure 6e) comprising Fe-oxides. Close to the fault zone, Fe-oxides occur within the serpentinites (Figure 6f).

3.5. Sedimentary Rocks from the Hyperextended Domain

To investigate the paleofluid flow that can affect the sedimentary basins in the hyperextended domain, we selected ODP Sites 638 and 641 from the Iberia distal margin [68] (Figure 1a). These sites provide a unique dataset documenting a syn-rift sedimentary section in a supra-detachment basin floored by hyperextended crust. The studied sedimentary sequence is characterized by syn-rift sediments deposited from Valanginian to Aptian times and post-rift sediments deposited during and after late Aptian [68]. The Valanginian layer is composed of sandstones interbedded with claystones. The Hauterivian section is made of claystone at the base, grading up-section to marlstones originating from slump deposits. The Barremian section is mainly made of marlstones. The Aptian sequence is composed

of sedimentary breccias alternated with limestone/marlstone and calcarenite beds. The Albian claystones, shales and black shales characterize the post-tectonic sequence.

At the Tasna OCT, tectono-sedimentary breccias (Figure 4(a2)) directly overlie the detachment fault. They are characterized by tectonic deformation but also show local evidence of a coeval sedimentary origin, such as millimetric layers of very thin sandstones and locally centimetric graded beds. Therefore, these breccias have a local source and the sedimentary transport is negligible. The tectono-sedimentary breccias are cemented by silica. The rims of the clasts are often made of second-phase quartz that is interpreted as the result of silica-enriched fluid migration. Because of these characteristics and the reworking of footwall-derived material, the tectono-sedimentary breccias are likely related to exhumation. Field relationships and detrital zircons indicate that a thin sedimentary layer (Tonschiefer Fm.) overlaying the tectono-sedimentary breccias is Late Jurassic in age [34]. The lack of a thicker sedimentary layer related to exhumation at Tasna may either indicate that the OCT was sediment-starved and/or that Tasna represented a structural high. Both observations are comparable to what was documented by the ODP Site 1067 at Hobby High along the Iberia margin [34,47].

We did not analyze the sedimentary rocks related to hyperextension in the Mauléon Basin, since no studies exist where the immediate supra-detachment sedimentary rocks in this basin are systematically analyzed using geochemical methods. However, two types of sedimentary rocks are important for understanding the fluid circulation along the NMD system. The first one encompasses the tecto-sedimentary breccias overlying the NMD (Figure 6b). They are intensely cemented by SiO₂ and their matrix is enriched in Fe-oxides. The second one comprises the pre-rift sandstones of the Triassic age that overlie the NMD. They show a series of Fe-oxides (± 5 cm thick) composed of hematite and goethite. Our field observations show that these veins are limited to areas where the pre-rift Triassic sequence is related to the NMD (Figure 6g).

4. Geochemical Data and Mass Balance Calculation

4.1. Geochemical Data

Bulk-rock chemical analyses were performed on fault rocks. They were obtained from samples digested using Li-tetraborate fusion, followed by dissolution in HNO₃-glycerol. At LHyGeS (CNRS-University of Strasbourg), Strasbourg, France, the samples were dried at 100 °C, re-weighed and ignited at 1000 °C for Loss on Ignition (% LOI). Approximately 100 mg of the sample was mixed with 750 mg of lithium tetraborate and melted at ~1000 °C. The melt was dissolved in an HNO₃-glycerol solution and analyzed by mass spectrometry. At LHyGeS, the concentrations were measured with a Thermo Scientific® ICP-AES and a Thermo Scientific® X Series 2 ICP-MS equipped with collision/reaction cell technology from the ThermoFisher Scientific company. SARM-Laboratory (CNRS-Nancy), Nancy, France data are from an ICP-MS Agilent 7700X and ICP-OES Thermo Fischer® ICP 6500 from the ThermoFisher Scientific company. The precision and accuracy of the method were routinely assessed by replicate analyses of the international rock standards [69] at both LHyGeS and SARM-Laboratories. Similar procedures were run by Acme Laboratory, Vancouver, Canada, with the same equipment from SARM laboratories. Total carbon and sulfur were analyzed using Leco equipment (Acme). The achieved precisions for major elements were <2% for concentrations >2%, <5% for the concentrations between 2 and 0.1%, and 10% for the lowest concentrations <0.1%. The precisions for trace elements were <2% for concentrations >100 ppm, <5% for concentrations between 100 and 0 ppm, and <10% for concentrations <10 ppm. According to the trace elements, the detection limits range from 1 ppm to 0.1 ppm. The element concentrations presented here and used in the study are above the given detection limits. The analyses of serpentinitized peridotites and their minerals were from Müntener et al. [70], who used the approach and laboratory (SARM-Nancy) described above. The whole-rock analysis of fault rocks from Iberia was conducted using the shipboard X-ray fluorescence [46] and the data from sedimentary rocks were obtained using X-ray diffraction (see [71]).

4.2. Gain and Losses of Element Calculations

The gain (enrichment) and loss (depletion) of elements during mantle exhumation and fault rock formation were calculated using the method proposed by Ague and Van Haren [72]. This considers the mass and volume changes in a metasomatically altered rock relative to its protolith. As a result, one can obtain the time-integrated effect of all metasomatism that a given altered rock or suite of altered rock underwent.

Usually, the mass balance analysis assumes that volume strain and mass changes have a normal (Gaussian) distribution, but these distributions can be highly skewed. Assuming a normal distribution for compositional data can be misleading, especially when accounting for mass balance [72]. Therefore, we chose the Monte Carlo-based bootstrap approach, which estimates data distribution instead of assuming any a priori statistical behavior [72]. The main idea of this method is to generate many virtual samples (the “bootstrap” samples) by averaging randomly chosen real data, in order to obtain enough samples to calculate the mass and volume changes and visualize their statistical probabilities. This approach allows for the confidence intervals for any result to be accessed, thus providing a detailed, data-driven, statistical distribution, especially in studies with few available samples (see Figure 1 in [72]).

The main workflow applied to both protoliths and altered samples consists of the following steps: (1) use Monte Carlo to randomly choose N laboratory samples, which can be included more than once at each realization; (2) calculate the average from the N chosen samples to generate a new virtual (i.e., bootstrap) sample (see Gain and Losses of Elements Calculations in Supplementary Material for details).

Let C_1, C_2, \dots, C_M be the concentrations of each constituent in the bootstrap samples. The mass and volume changes in each protolith-altered pair transformation can be obtained as follows:

$$\hat{\tau}^{j*} = \left(\frac{\bar{C}_i^{0*}}{\bar{C}_i^{j*}} \right) \left(\frac{\bar{C}_j^{i*}}{\bar{C}_j^{0*}} \right) - 1 \quad (1)$$

$$\hat{\varepsilon}^* = \left(\frac{\bar{C}_i^{0*}}{\bar{C}_i^{j*}} \right) \left(\frac{\bar{\rho}_j^{0*}}{\bar{\rho}_j^{j*}} \right) - 1 \quad (2)$$

where $\hat{\tau}^{j*}$ and $\hat{\varepsilon}$ refer to mass and volumetric changes, respectively; \bar{C}_i^{0*} , \bar{C}_i^{j*} , \bar{C}_j^{i*} and \bar{C}_j^{0*} are the concentrations of the original (o), altered (') of the immobile (i) and mobile (j) species; $\bar{\rho}_j^{0*}$ and $\bar{\rho}_j^{j*}$ are densities of original and altered mobile species; the (*) index represents the bootstrap sample.

These calculations were applied a few thousand times to obtain a robust, data-based statistical inference for the mass changes in each constituent, in addition to bulk mass and volume changes. Figure 7 presents an example of an analysis of the bootstrap results. The cumulative distribution (dark blue line in Figure 7a,b) allows for the calculation of the percentiles that we used to build the box-plot (Figure 7c). The percentile 50, P_{50} is the median of the results, which is assumed to be the measure of the central tendency (orange line in Figure 7c). Percentiles 25 (P_{25}) and 75 (P_{75}) define the 50% confidence interval, meaning that there is a 50% probability that a bootstrap realization result falls between P_{25} and P_{75} , and delineate the center of the distribution, as depicted by the rectangular black box in the box plot. Finally, $P_{2.5}$ and $P_{97.5}$ mark the 95% confidence interval, namely, the interval with a 95% probability of containing a bootstrap realization. This interval is represented by the whiskers in the boxplot. Any realization outside the 95% confidence interval is considered an outlier (open circles in Figure 7c). The boxplots for each constituent can be plotted together, facilitating the visualization of the main result (Figure 7c). We regard mass change as statistically relevant if the confidence interval is far from zero.

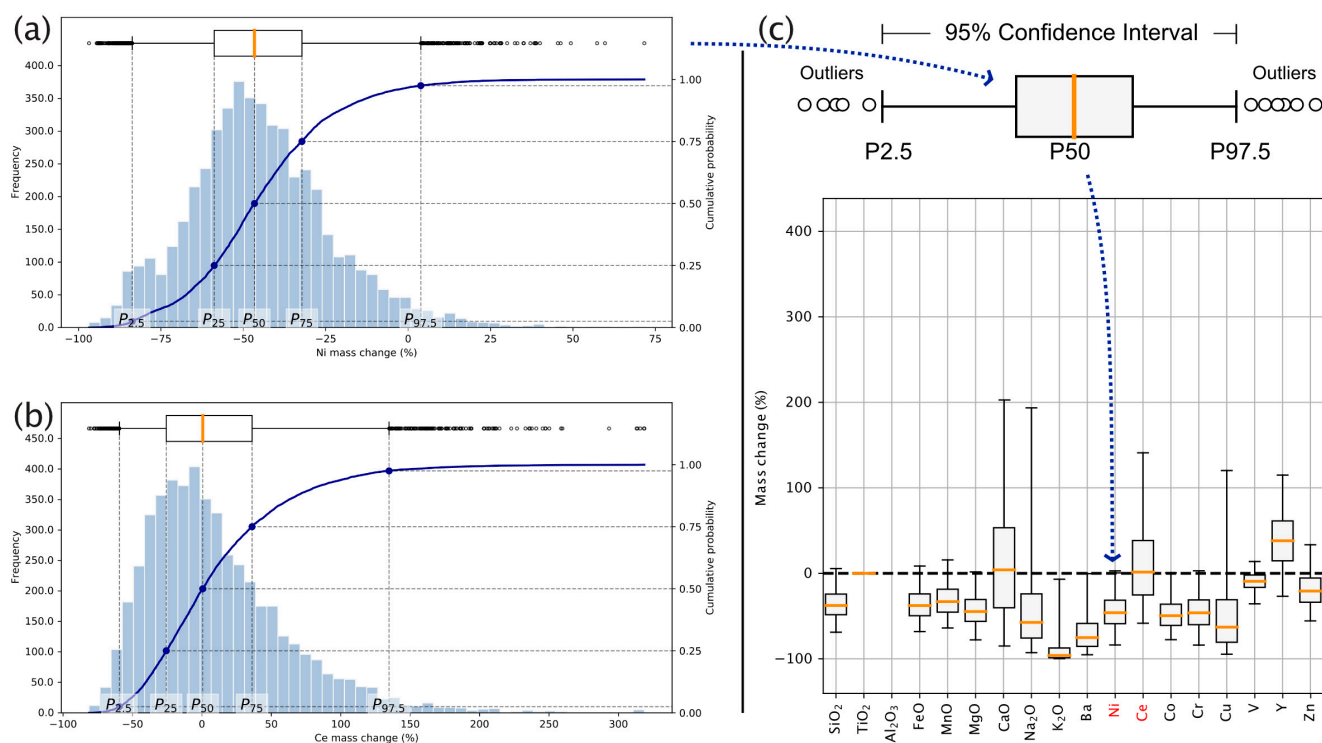


Figure 7. Reading the bootstrap results. An example of how to read the results is shown based on the serpentinization result. Subfigures (a,b) are detailed species (Ni and Ce) distributions, showing the probabilities of gain and losses. Note the confidence interval (black box with orange line centered in P_{50}). Subfigure (c) shows only the confidence interval (without outliers) for each species, allowing for us to plot all species in one chart for an overall analysis. Note the dotted blue arrow showing the extraction of each confidence interval (e.g., Ni and Ce) from (a,b) which allow to build the mass change chart (c). Note Ni and Ce with red letters in (c). The range spanned by the whiskers represents the 95% confidence interval, while the black box marks the 50% confidence interval. Serpentinization will most likely result in a loss in probability distribution such as Ni (a), where the confidence interval is far from zero. On the other hand, when the confidence interval is fairly centered around zero, mass changes are not statistically relevant in the serpentinization process, such as Ce (b). See the text for explanations.

Another important point regarding the mass and volume calculations is to choose the elements or constituents as a geochemical reference frame. Usually, elements are discarded when they are part of the altered minerals and veins, when there is high variation among the samples and when the results have large uncertainties related to analytical problems. MacLean and Barrett [73] showed that elements such as Al, Ti and Zr can be used as immobile elements for many geological processes, including hydrothermal alteration. Immobility can be verified if these elements show a good linear correlation between selected protolith and altered rocks (see Figure 5 in [4]).

5. Analysis of Geochemical Data: Results

5.1. Mantle Rocks

The geochemical data (ICP-MS/AES and XRF analyses) of serpentinites from the OCTs of the Alpine Tethys with different degrees of serpentinization [4,70] were used to determine chemical transfer during serpentinization. Note that, in the studied examples, non-serpentinized mantle rocks do not exist. Therefore, we used little serpentinized mantle rocks (between 2 and 10%) as protoliths. The method of Ague and Van Haren [72], as described above, enabled us to calculate the mass balance between the weakly serpentinized peridotites (between 2 and 10% of serpentinization) and more strongly serpentinized peridotites (between 10% and 95% of serpentinization). This approach differs from that

applied by [4] and is more reliable since it allows for access to the confidence intervals for any result.

Figure 7a shows a histogram (light blue bar plot) of 5000 Monte Carlo realizations for the Ni mass change performed by randomly combining five lab measurements of protoliths and 40 altered samples. This indicates that mantle rock alterations will most likely result in a Ni loss (Figure 7a). On the other hand, Figure 7b shows the same analysis for Ce, where we see the 95% confidence interval fairly centered around zero, indicating that Ce mass changes are not statistically relevant in alteration processes.

Figure 8a shows the total gain and loss of elements from weakly to moderate and highly serpentinized rocks. This chart is the result of the bootstrap method, considering Al_2O_3 and TiO_2 as an immobile reference frame (option B from Ague and Van Haren [72]; see Supporting Information for details). The choice of Al_2O_3 and TiO_2 is based on previous mass balance studies of similar rocks from the Err detachment system [4]. The use of these elements as “immobile” provides results coherent with petrological and mineralogical observations (for discussions, see [4,74]). The horizontal line at a percentage of zero marks the level of no mass change. Species below and above that horizontal line show losses or gains, respectively. In these charts, Si, Mg, Ca, Fe, Mn, and the trace elements Ni, Cr and V are some of the main elements lost during the alterations in the subcontinental peridotites along the OCT of the Alpine Tethys. In Figure 8, some elements can be seen as loss and gain, depending on the pairs of protolith/ altered rock considered in the 5000 Monte Carlo realization, which can be also seen as the stage of alteration. Note that the peridotites from the OCT in the Alps are more enriched than those from MORs. Figure 9 details mass change histograms for these species, with the 95% confidence interval dominated by losses. In many examples, the P_{50} is between -45% and -35% , as is the case of SiO_2 , MgO , FeO , MnO , Cr and Ni. The loss of elements, particularly those elements characteristic of the mantle, which are rarely found in continental basements (e.g., Cr, Ni and V), enables us to use them as tracer elements for mantle-reacted fluids (see also [4]). A possible origin from extrusive magmatic rocks can be excluded, since such rocks do not exist in the studied areas.

In the Iberia margin, the subcontinental exhumed peridotites are more than 90% serpentinized and their composition has main chemical characteristics similar to serpentinites from the Alps, i.e., they are depleted in Ni, Cr, V, Si, Mg, Ca, Fe and Mn (e.g., Hebert et al. [75]). Chemical analyses performed on veins of chrysotile, lizardite and calcite from the fault rocks of the Iberian OCT (ODP Site 1068) exhibit an elevated content of metal, e.g., Ni, Fe and, to a lesser extent, Cr and Co [66], showing their mobile behavior. The serpentinites from the Mauléon Basin show a wide range of serpentinization [76]. Like the serpentinites from the Alps, the higher the degree of the serpentinization of peridotites, the lower the concentration in elements such as Ni, Fe and Mg.

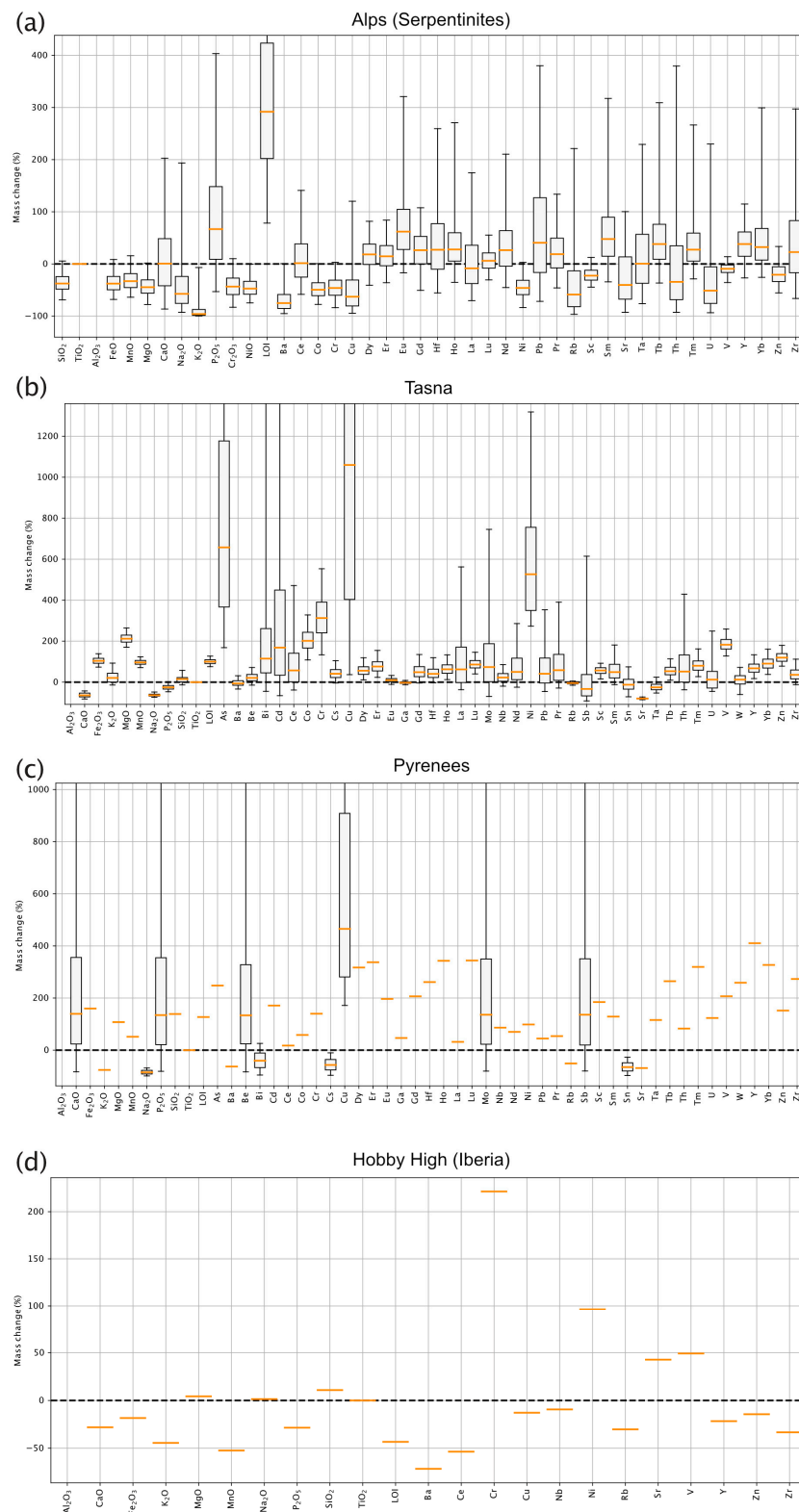


Figure 8. Gain and loss of elements in mantle and continental crust rocks. The diagrams show the gains and losses of species (i.e., chemical elements and compounds) related to transformation (alteration) from protoliths to altered rocks. Protoliths are unaltered/weakly altered continental crust rocks, or less deformed fault rocks and peridotites, or weakly serpentinized peridotites. Altered rocks are fault rocks over the continental crust and serpentinized peridotites. Orange lines are P₅₀ (see Figure 7 for explanation) or in some cases, when the mass balance is performed with one protolith and one altered rock, they represent the deterministic result (i.e., without statistic calculation). (a) Gain and

loss related to peridotite and serpentinite alterations. Note the loss of species such as Ni, Cr, V, Si, Mg, Ca, Fe and Mn below the zero-mass change. **(b–d)** is the gain and loss from the basement of the continental crust to fault rock. Note that species such as Ni, Cr and V, which are lost during peridotite and serpentinite alterations, are the same species gained in fault rocks from extensional detachment systems in the continental crust. Data from Table 1. **(b)** Mass change assuming granite from Middle Err as a protolith and cataclasites and gouges as altered rock from the UTD at Tasna OCT. **(c)** Mass change from paragneisses to cataclasites from Pic de Garralda (Mauléon Basin). **(d)** Mass change from HHD-1 (cataclasites) to HHD-2 (gouge/ fault breccia) in the Hobby High Detachment at Iberia OCT. We used Table 1 to present the geochemical data from fault and continental crust basement rocks, and published data from [70] and [4] for serpentinitized peridotite rocks.

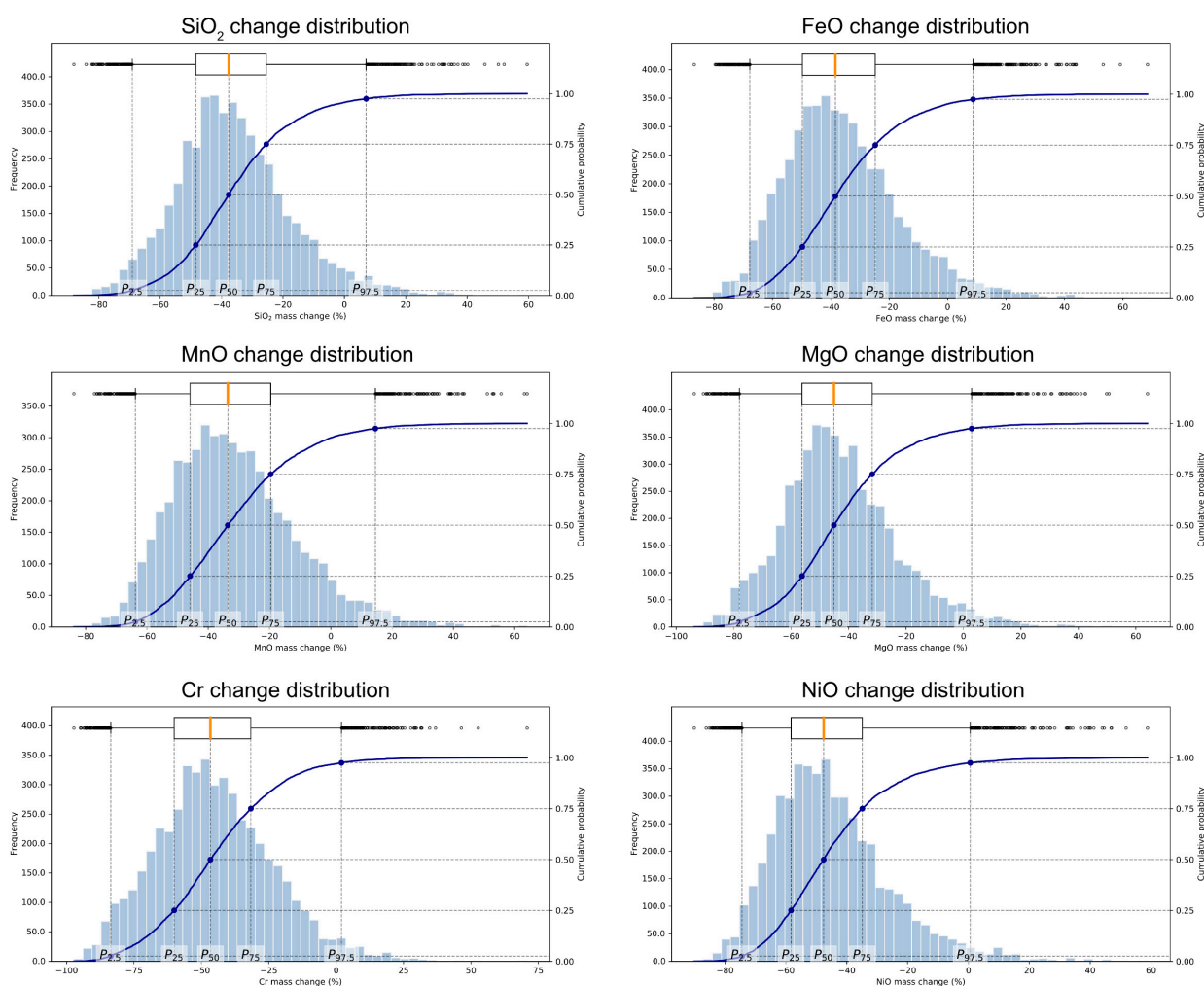


Figure 9. Frequency distribution and percentile estimations of some species related to the serpentinization processes. Summary of the Monte Carlo mass change simulations. Vertical bars represent the histogram of the results; the solid blue line is the cumulative probability density function; the box depicts the 95% confidence interval (our measure of variability) around the median (P₅₀), marked by the orange line. Note that these species have a high probability of being lost during peridotite and serpentinite alterations.

Table 1. Bulk rock geochemistry of continental crust and fault rocks.

Sample Lithologie Unit Site Lab	*	VA-T3-07 go Tasna Mot de Ri Acme	VA-T3-20 go Tasna Mot de Ri Acme	T-7-rt go Tasna Mot de Ri SARM	VA-T2-09 go Tasna Mot de Ri SARM	VA-T2-08 ca Tasna Mot de Ri SARM	VA-T3-18 chl-sch-cat Tasna Mot de Ri Acme	VA-L-9a Granite Middle Err Laviner SARM	VA-L-9b Granite Middle Err Laviner LHyGeS	VA-B13-1 Granite Middle Err Val Bever ACME	VP-GAR-03.B ca Mauléon P. Garralda SARM	VP-GAR-03.B ca Mauléon P. Garralda SARM	VP-GAR-01.A Paragneiss Mauléon P. Garralda SARM	VP-GAR-01.A Paragneiss Mauléon P. Garralda SARM	HHD-2 go Hobby High 19R-2 114–116 cm ODP	HHD-1 ca Hobby High 18R-1 91–93 cm ODP
Al ₂ O ₃	%	15.52	15.45	17.00	16.20	16.56	10.86	15.84	15.80	20.59	1.16	1.16	2.97	2.97	15.89	16.12
CaO	%	1.00	0.88	0.98	0.87	0.67	0.51	1.53	1.64	6.13	<0.03	<0.03	<0.03	<0.03	9.40	13.17
Fe ₂ O ₃	%	6.40	7.25	7.28	6.36	6.24	4.85	2.70	3.14	4.89	2.26	2.26	2.03	2.03	9.52	11.75
K ₂ O	%	3.14	3.53	4.70	3.53	4.36	2.51	3.88	3.82	2.35	0.05	0.05	0.51	0.51	0.75	1.36
MgO	%	2.95	4.13	3.69	4.19	3.18	1.94	1.05	1.04	1.41	0.51	0.51	0.57	0.57	5.26	5.08
MnO	%	0.07	0.10	0.11	0.09	0.09	0.06	0.04	0.05	0.06	0.00	0.00	0.01	0.01	0.17	0.36
Na ₂ O	%	2.33	1.26	1.27	0.84	1.50	0.99	4.03	3.83	3.96	<0.01	<0.01	0.07	0.07	4.30	4.27
P ₂ O ₅	%	0.17	0.16	0.16	0.14	0.12	0.06	0.17	0.23	0.18	<0.04	<0.04	<0.04	<0.04	0.22	0.31
SiO ₂	%	64.33	62.35	61.80	61.97	63.13	74.79	67.45	67.60	56.87	93.84	93.84	92.02	92.02	51.97	47.22
TiO ₂	%	0.51	0.92	1.01	0.79	0.75	0.75	0.32	0.38	0.62	0.22	0.22	0.26	0.26	1.87	1.77
LOI	%	3.40	3.70	3.75	4.21	4.05	2.50	1.78	1.61	2.70	0.97	0.97	1.00	1.00	5.70	10.13
As	ppm	7.70	8.00	*	4.83	3.44	6.70	2.13	*	<0.5	3.19	3.19	2.14	2.14	*	*
Ba	ppm	380.00	654.00	828.70	671.10	731.90	489.00	724.80	820.90	602.00	13.46	13.46	85.02	85.02	46.00	163.00
Be	ppm	3.00	3.00	*	3.36	1.82	2.00	2.77	*	2.00	<0.4	<0.4	<0.4	<0.4	*	*
Bi	ppm	0.20	<0.1	*	<0.1	0.13	0.10	<0.1	*	<0.1	<0.1	<0.1	0.18	0.18	*	*
Cd	ppm	1.00	<0.1	1.00	0.33	0.14	<0.1	<0.12	0.30	<0.1	0.25	0.25	0.22	0.22	*	*
Ce	ppm	45.70	67.50	134.00	70.49	84.99	80.50	77.35	118.00	16.60	14.79	14.79	29.45	29.45	41.00	89.00
Co	ppm	21.80	13.00	20.20	17.97	10.89	12.40	3.95	7.00	6.80	2.72	2.72	4.02	4.02	*	*
Cr	ppm	41.05	68.42	126.60	130.00	79.12	61.58	15.00	31.70	20.53	22.30	22.30	21.76	21.76	367.00	115.00
Cs	ppm	5.00	2.00	2.61	3.74	2.98	2.10	1.79	1.81	3.80	<0.1	<0.1	0.25	0.25	*	*
Cu	ppm	195.70	25.10	41.90	31.79	12.90	16.50	<0.5	24.70	5.60	5.54	5.54	<5	<5	45.00	52.00
Dy	ppm	8.43	4.78	6.60	4.45	3.47	3.89	3.08	4.08	3.70	2.71	2.71	1.52	1.52	*	*
Er	ppm	4.92	2.57	3.74	2.36	1.86	2.23	1.34	1.92	2.10	1.66	1.66	0.89	0.89	*	*
Eu	ppm	1.70	1.36	1.96	1.19	1.28	1.13	1.20	1.48	1.65	0.44	0.44	0.35	0.35	*	*
Ga	ppm	18.90	19.40	*	22.21	24.25	14.10	20.07	*	24.80	2.54	2.54	4.05	4.05	*	*
Gd	ppm	8.30	5.92	9.30	5.21	4.78	5.17	4.29	6.38	3.65	2.09	2.09	1.60	1.60	*	*
Hf	ppm	4.10	6.10	10.63	5.39	6.82	8.60	3.71	5.01	7.50	9.76	9.76	6.32	6.32	*	*
Ho	ppm	1.61	0.97	1.41	0.85	0.64	0.76	0.51	0.77	0.61	0.61	0.61	0.32	0.32	*	*
La	ppm	30.40	34.80	67.52	35.89	41.46	38.50	40.00	62.61	7.60	7.92	7.92	14.06	14.06	*	*
Lu	ppm	0.51	0.37	0.54	0.36	0.30	0.34	0.17	0.23	0.33	0.29	0.29	0.16	0.16	*	*
Mo	ppm	<0.1	0.60	1.80	<0.5	0.52	0.20	<0.5	*	0.20	<0.5	<0.5	<0.5	<0.5	*	*
Nb	ppm	9.80	12.90	18.68	12.26	13.32	12.10	11.01	16.03	9.40	3.59	3.59	4.51	4.51	9.00	10.00
Nd	ppm	30.90	31.40	57.46	31.67	35.59	35.30	31.19	47.27	11.90	8.31	8.31	11.43	11.43	*	*
Ni	ppm	50.60	35.10	46.00	48.15	34.98	30.30	9.78	10.00	3.60	7.75	7.75	9.13	9.13	78.00	40.00
Pb	ppm	17.60	18.80	50.80	22.07	9.67	10.70	17.86	30.20	5.20	2.65	2.65	4.29	4.29	*	*
Pr	ppm	7.39	8.26	15.40	8.37	9.82	9.39	8.61	13.10	2.42	2.08	2.08	3.16	3.16	*	*
Rb	ppm	115.90	105.00	122.10	127.50	120.60	81.70	115.70	133.60	141.00	3.46	3.46	16.59	16.59	9.00	13.00
Sb	ppm	<0.1	<0.1	0.40	<0.2	<0.2	<0.1	<0.2	0.50	<0.1	<0.2	<0.2	<0.2	<0.2	*	*
Sc	ppm	8.00	15.00	15.60	16.37	15.28	10.00	7.30	8.46	13.00	2.48	2.48	2.04	2.04	*	*
Sm	ppm	7.46	6.29	11.01	6.20	6.72	6.44	5.63	8.20	3.26	1.97	1.97	2.02	2.02	*	*
Sn	ppm	3.00	3.00	3.70	1.61	1.55	<1	1.19	2.70	4.00	<0.45	<0.45	1.37	1.37	*	*
Sr	ppm	73.60	28.10	40.00	41.80	52.36	38.60	204.50	207.30	340.50	6.84	6.84	51.21	51.21	275.00	194.00
Ta	ppm	0.70	0.80	1.72	0.94	0.97	0.60	1.27	1.87	1.00	0.36	0.36	0.39	0.39	*	*
Tb	ppm	1.37	0.90	1.26	0.77	0.66	0.72	0.59	0.77	0.64	0.39	0.39	0.25	0.25	*	*
Th	ppm	8.50	10.60	21.90	11.47	17.01	14.50	14.19	19.80	3.10	4.26	4.26	5.45	5.45	*	*
Tm	ppm	0.68	0.38	0.55	0.34	0.28	0.33	0.18	0.26	0.34	0.25	0.25	0.14	0.14	*	*
U	ppm	30.60	2.30	2.05	1.57	1.61	1.70	2.04	2.64	4.40	0.86	0.86	0.90	0.90	*	*
V	ppm	91.00	119.00	127.20	108.50	102.10	71.00	28.25	37.50	59.00	23.32	23.32	17.79	17.79	397.00	268.00
W	ppm	0.60	0.90	1.30	1.64	0.82	<0.5	0.70	*	0.90	0.91	0.91	0.59	0.59	*	*
Y	ppm	45.00	28.10	37.70	25.73	18.05	20.20	15.36	20.60	19.60	18.53	18.53	8.50	8.50	28.00	36.00
Yb	ppm	3.84	2.52	3.54	2.27	1.89	2.32	1.15	1.57	2.07	1.74	1.74	0.96	0.96	*	*
Zn	ppm	155.00	88.00	83.00	115.50	118.50	65.00	44.32	47.90	61.00	18.07	18.07	16.79	16.79	85.00	100.00
Zr	ppm	164.40	230.10	349.40	201.10	253.80	327.00	145.80	159.70	347.20	403.50	403.50	253.10	253.10	137.00	207.00

ca: cataclasite also refers to foliated cataclasites; go: gouge; chl-sch-cat: chlorite schist cataclasite. Major elements (oxides) and LOI are in %wt and trace elements are in ppm. Analyses from the Hobby High are from the matrix part; data from from Whitmarsh et al. (1998). The * indicate elements not analyzed, <L.D. means values lower than the detection limit. Samples from SARM, ACME and LHyGeS was performed using ICP and samples from ODP were analyzed using XRF (see Methods for details). Whitmarsh et al. [46].

5.2. Continental Crustal Fault Rocks

The bulk compositions of the fault rocks of the three extensional detachment faults from Hobby High off Iberia, Tasna OCT in the Alps and the NMD in the Mauléon Basin were analyzed with ICP-AES/MS and XRF methods (Table 1). We used the method of Ague and Van Haren [72] to quantify elements that either entered the fault zone (gains) or left the fault zone (losses). For the calculations, we used Option B [72], with Al_2O_3 and TiO_2 as immobile elements (see supporting information), and the granite samples for Tasna, the paragneisses from Pyrenees, and the cataclasite for the Hobby High (see lithology name in Table 1 and Figure 2 for location) as a protolith.

In the fault rocks drilled at Hobby High (ODP Site 1067) and sampled along the UTD of the Tasna OCT and the NMD in the Mauléon Basin, a systematic and elevated gain in elements such as Ni, Cr and V is observed (Figure 8b–d). These gains are in agreement with results from the Err extensional detachment system [4,74]. Such gains are not observed in more continent-ward extensional detachment systems in the Alpine Tethys examples [4]; therefore, they are useful fingerprints for tracing mantle-reacted fluids in the distal margin.

5.3. Sedimentary Rocks from Supra-Detachment Basins

Geochemical results from Clauser et al. [71] sampled on the ODP Sites 638B and 641C (Figure 1a) are used to evaluate if there is a fluid signature in the sedimentary rocks related to the formation of hyperextended domains and exhumation of mantle rocks (Figure 10). The existing compounds or ratios were used as follows:

(1) CaCO_3 content profile allows for us to distinguish between carbonate- and siliclastic rocks. (2) Sr is often ascribed to both carbonates—substituting Ca—and clay minerals—as byproducts of feldspar alterations. In marine calcareous deposits, Sr/Ca and Mg/Sr ratios tend to mirror the CaCO_3 trend, even when considering diagenetic alterations [77–79]. (3) High concentrations of Mg and Fe are commonly correlated with clay mineral abundance; both are common in phyllosilicates (e.g., chlorite) and point to a clastic detrital origin of the sediments. (4) Mn/Fe ratios range between 0.5 and 1 in siliclastic rocks. Mn is a minor element in clay and rare in carbonate minerals. Mn enrichment is uncommon in normal depositional hemipelagic settings, and is often attributed to hydrothermal activity or a long depositional hiatus.

CaCO_3 contents of the ODP Site 638B section reflect the variation in lithologies, especially in the Late Valanginian to Early Hauterivian section where intercalations of thin sandy turbidites and marlstones are frequent. The clay mineral association in these layers is prevalent in chlorite, kaolinite and illite [80]. The variation in the Mg/Sr ratio usually follows the CaCO_3 trend. The exception is the increase in Mg/Sr corresponding to the clay-rich facies (e.g., at ~345 m below seafloor (mbsf) or dolomite clast (at 382.8 mbsf). However, the higher Mg/Sr at ~210 mbsf, linked to an increase in Mg (~1.5–2 times higher) relative to the CaCO_3 and Sr contents (Table 1 in [71]), is not due to a change in the main marlstone lithology but to an external contribution. In this site, the Mn/Fe ratio does not change much, remaining constant at values around 0.7–1.

At the ODP Site 641C, in the Barremian to Early Aptian section, there were no large discrepancies between Sr/Ca, Mg/Sr and CaCO_3 trends (Figure 10). Likewise, the Mn/Fe ratio changes very little. However, sedimentary rocks from Early Aptian to Late Aptian–Early Albian record an increase in the Mg/Sr ratio (higher Mg content), while CaCO_3 values decrease significantly. This is accompanied by a higher Mn/Fe ratio. The observed increase in Mg and Mn contents is not related to facies variation, since the Aptian sedimentary sequence comprises carbonate marlstones and thin limestones. At the same interval, and as a single level (e.g., ~10 m-thick section 641C-8R-CC to 9R-2), silicified carbonates and authigenic quartz pore-filling cements are described to be enriched in Fe and Mn [81]. Therefore, it is necessary to evoke an external source, different from the detrital one, in order to explain such enrichments and silicification in this specific sedimentary section.

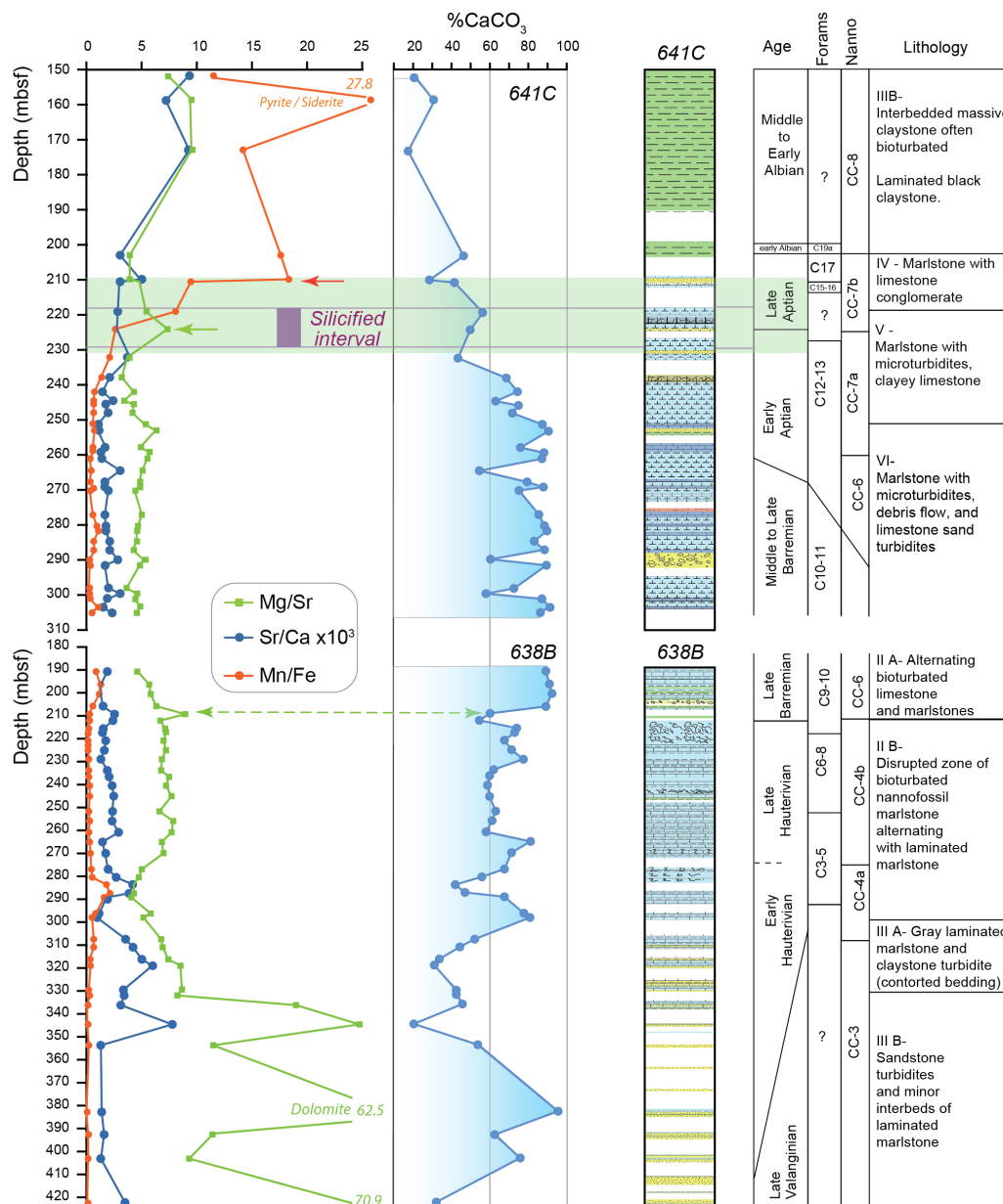


Figure 10. Geochemical variations in Mn/Fe, Sr/Ca and Mg/Sr from ODP Sites 638B and 641C. Note the enrichment of Mn, Mg and Si in rocks of Late Aptian age corresponding to the timing of mantle exhumation. Colored arrows indicate the samples described in the text. Data from Clauser et al. [71].

6. Discussion

6.1. Evidence for Fluid Flow during Hyperextension and Mantle Exhumation

First-order evidence for fluid flow during hyperextension and mantle exhumation is the formation of syn-kinematic hydrated minerals such as serpentinite, chlorite, illite and sericite along detachment faults related to the breakdown of feldspars and olivine, as well as the multi-stage syn-extensional veining of chrysotile, lizardite, chlorite, epidote and calcite observed in OCTs (Figure 4b,g–i and Figure 5d–f).

Fluid flow during hyperextension and mantle exhumation is likely linked to hydrothermal systems (e.g., [64,66,82]). In such systems, cold seawater infiltrates downward through hot, brittle exhuming continental and mantle rocks, creating convective cells incorporating elements or species that are released from the hydrating and deforming rocks in the reacted fluid (Figures 8, 9 and 11). The hot fluids rise along detachments and across the hyperextended continental crust before returning to the seafloor (Figure 11). This is best

demonstrated by the loss of Ni, Cr and V from the altered peridotites and serpentinites, mirrored by a gain of the same elements in syn-kinematic minerals (mainly chlorite) along extensional detachment faults in the crust and the overlying syn-rift sedimentary rocks ([4]; see Section 6.3 for further discussion). This process is well-recorded in the Alpine Tethys OCTs, where serpentinites enriched in Fe-oxide show also a high Barium content (~9 wt%) and hydrothermally formed chlorite [4]. Perseil and Latouche [82] described hydrothermal mineralizations in ultramafic rocks overlain by hydrothermal cherts. At the ODP Site 1068 at the Iberia margin (Figure 5b), Beard and Hopkinson [66] concluded, based on the geochemistry and mineralogy of the fault rocks in the serpentinized mantle, that mantle exhumation in the OCT was linked to ultramafic–hydrothermal venting.

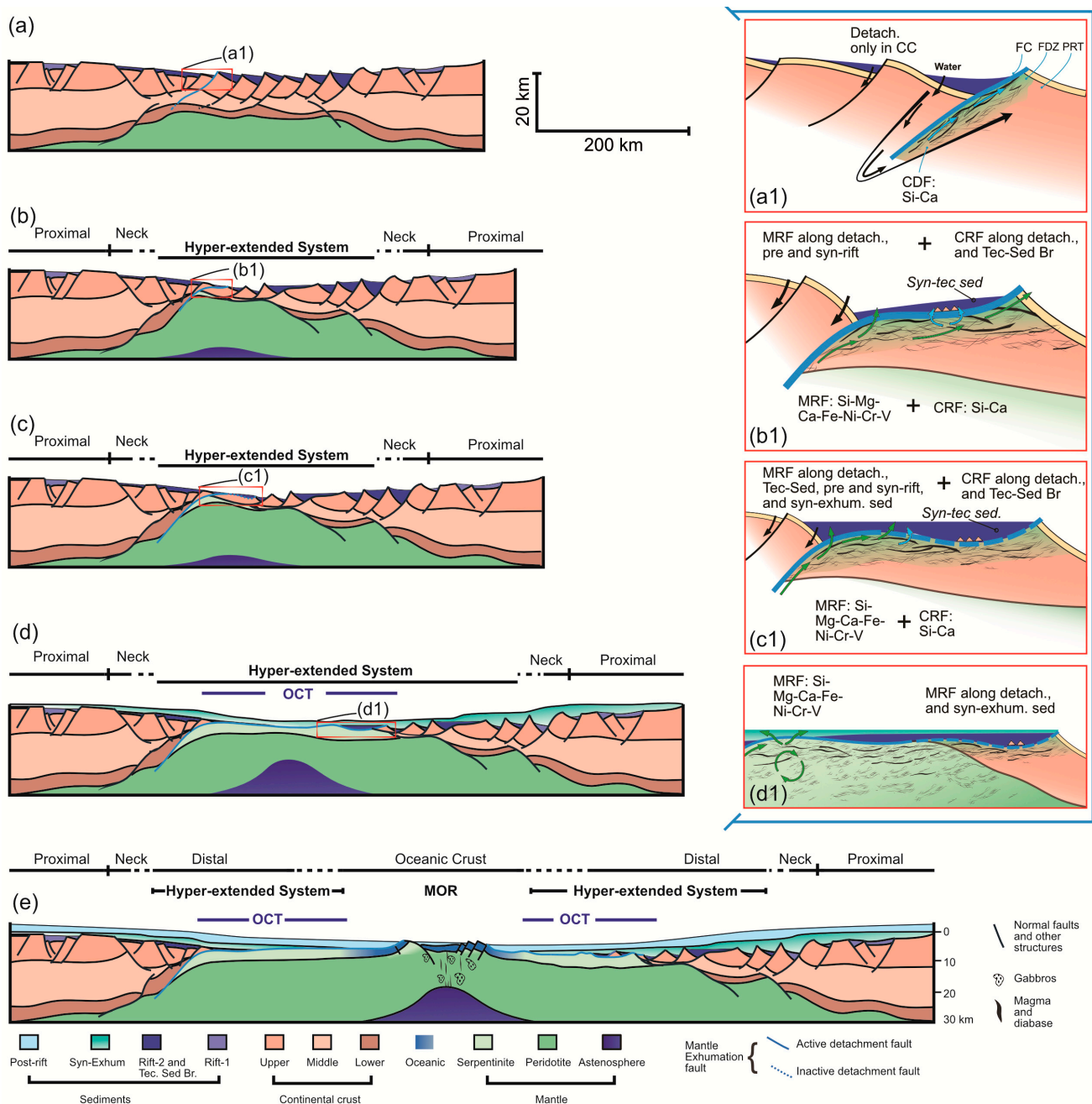


Figure 11. Formation and migration of mantle-reacted fluids (MRF) and continental-crust-reacted fluids (CRF). (a,a1) Seawater migrates downward through high-angle normal faults in the hanging

wall of an extensional detachment fault system during its activity. This triggers fluid–rock interactions and alteration processes such as saussurization/albitization in the fault zone within the thinned continental crust. These processes form the CRF, which migrates through the detachment fault systems and can be recorded in the syn-tectonic sedimentary sequence where we include the tectono-sedimentary breccias, represented by small triangles (**b,b1**). Note that, at this stage, serpentinization starts below the thinned continental crust and MRF starts to migrate along the fault zone of the active detachment, reaching the pre- and syn-tectonic sediments. (**c,c1**) CRF is no longer recorded in the inactive segment of the detachment fault (dashed blue line) but is recorded further outboard (continuous blue line). (**d,d1**) The segment of the detachment fault is inactive over the continental crust, and the deformation, as well as fluid flow, is focused on the zone in which the mantle is exhumed. At this stage, MRF pollutes the seawater and interacts with syn-exhumation sediments. (**e**) Onset of seafloor spreading. Deformation ceased in the continent and MRF is no longer recorded in the hyperextended rifted margin. Eventually, it can become active during the formation of Oceanic Core Complexes at MOR, away from the OCT. FC: fault core, FDZ: fault damage zone; PRT: protolith; Tec-Sed Br: tectono-sedimentary breccias, syn-tec sed: syn-tectonic sediments, syn-exhum. sed: syn-exhumation sediments.

These observations allow us to conclude that hyperextension and mantle exhumation are linked to the intense migration of seawater along faults, resulting in alterations in crustal and mantle rocks and the leaching of elements such as Si, Mg, Ca, Fe, Mn, Ni, Cr and V (Figures 8a, 9 and 10). In this study, we distinguish between “mantle-reacted fluids” assigned to fluids that show high concentrations of trace metals (Ni, Cr, V) and major elements (Si, Mg, Ca, Fe and Mn) and “continent-reacted fluids”: fluids enriched in Si and Ca without the enrichment of trace metals. In the discussion, we will first focus on the mantle-reacted fluids and their signature, then we will discuss their pathways and the origin of transferred mantle-derived elements, and, finally, we will propose a conceptual model for fluid flow in hyperextended, magma-poor margins.

6.2. Composition of Mantle-Reacted Fluids

The composition of mantle-reacted fluids can be indirectly constrained by the type of secondary minerals formed in fault zones related to mantle exhumation. The syn-kinematic hydrated minerals (e.g., serpentine and chlorite) forming the fault rock matrix and veins containing Fe-oxides and Fe-Ni alloys confirm that the damage zone of detachment faults in the mantle represents the main pathway for fluid migration. Mineralization, exemplified by spots of Fe-oxide in the serpentinites from the Pyrenees (Figure 6f) and from the Platta unit in the Alps where Fe-oxides often occur in serpentine and calcite veins, attests to an important circulation of Ca- and Fe-rich fluids [4,83]. The occurrence of Ni-Fe alloys, sulfide, andradite, hydroandradite and brucite in serpentine veins from the ODP Site 1068 (Figure 5b), is further evidence [66] for the migration of fluids enriched in Si, Fe, Mg and Ni. These observations prove that mantle-reacted fluid can transport many species, including Si, Ca, Mg, Fe, Ni, Cr and V (Figure 8), from the serpentinizing mantle, through the hyperextended crust, and towards the seafloor.

6.3. Fluid Pathways Recorded by Fault Rocks from Rift-Related Detachment Systems

Fluid migration in hyperextended systems is depicted by the neo-formation of syn-kinematic phyllosilicates and precipitation of quartz and calcite veins in fault rocks found along extensional detachments in the continental crust. As these veins are, in most cases, syn-kinematic, the migration and imprint of Si- and Ca-enriched fluids along the detachments occurs during ongoing fault activity. Secondary oxides and Fe-chlorite (red star in Figure 4a(a2)) are only found in fault rocks from detachment faults that root into the mantle. The gain of Fe (e.g., Figure 8b–d) along these detachments indicates the existence of an open fluid system with an external source of Fe (i.e., mantle-reacted fluids).

The migration of fluids along the detachment faults that root into the mantle (Figure 11) is also shown by the gain in “exotic” trace elements such as Ni, Cr and V that are rare

in the continental crust (Figure 8b–d). These elements are enriched in the syn-kinematic neo-formed phyllosilicates in the fault rocks (gouges, cataclasites) in the continental hyperextended crust. Pinto et al. [4] were among the first to interpret the enrichment of these trace metals (e.g., Ni, Cr and V) as proxies for mantle-reacted fluids in the hyperextended domain, mainly based on the following observations: (i) their concentrations in mantle rocks are a hundred times greater than in continental rocks, (ii) these elements are lost during mantle rock alteration, most likely due to alterations in the already serpentinized mantle, and retained in the fault rocks along extensional detachment systems that root into the mantle (Figure 8a–d), and (iii) they are not observed along rift-related fault systems in the more proximal parts of the margin, where faults terminate at mid-crustal decoupling levels. These points corroborate that fluid flow is focused along detachment systems that propagate into the mantle during hyperextension. They also demonstrate the existence of convective cells at a kilometer scale, connecting the marine reservoir with crustal and mantle rocks and triggering massive element transfer in hyperextended domains.

6.4. Signature of Mantle-Reacted Fluids Recorded in Syn-Hyperextension Sedimentary Rocks

High concentrations of mantle-derived elements such as Cr, Ni and V are not only observed along extensional detachment faults in the hyperextended continental crust, but also the syn-hyperextension sedimentary layers overlying the detachment faults that root into the mantle. This observation confirms that mantle-reacted fluids migrated upwards and reached the seafloor. If element transfer is linked to active detachment faulting, mantle-derived elements should only be found in syn-detachment/exhumation sedimentary rocks. At the Iberian margin, the Upper Aptian carbonates drilled at ODP Site 641 (Figures 1a and 10) were deposited during mantle exhumation. In these carbonates, Mg and Mn concentrations increase while CaCO₃ content stays constant. This increase cannot be explained by simple diagenesis. Thus, an additional source for Mg and Mn is required to explain the high concentrations of these elements. Similar relationships between Mg hydrothermal input in basal dolomitic sediments and mantle rocks have been established in other settings, such as the Tyrrhenian Sea [84].

In the hyperextended domain in the Mauléon Basin, veins of Fe-oxide/hydroxide cut through the Triassic pre-rift sedimentary rocks, indicating that the imprint of Fe-enriched fluids had to occur after the Triassic period (Figure 6g). It is also important to note that these veins are spatially linked to the NMD and related to mantle exhumation. Thus, like the observations reported from the Iberia example, it appears that extensional detachment systems may have acted as pathways for the mantle-reacted fluids migrating through sedimentary rocks overlying the NMD.

At the Iberia margin, in addition to the Mg and Mn, silicified levels (Figure 10) also occur in the Aptian section, which is syn-mantle exhumation [81]. This occurrence is unlikely to be related to saussuritization/albitization in the continental crust, since deformation and fault activity in the continental crust have ceased at that stage, as observed by the sealing of faults in the distal continental margin by the Aptian section [85]. Therefore, the transfer of Si may be related to mantle-reacted fluids; however, other sources cannot be excluded. The occurrence of Si-rich fluids is also found in the tectono-sedimentary breccias overlying the NMD in the Mauléon Basin and the UTD along the Tasna OCT. All these observations are compatible with the idea that Mg, and also Ni, Cr and V, were transferred out of the hydrating mantle, while Si, Fe and Mn may have had a mantle and continental source, and were enriched in pre- to syn-hyperextension/exhumation sediments.

6.5. Results of Mass Balance, Source of Elements and Related Processes

In this study, we present geological and geochemical evidence for mass transfer during hyperextension and mantle exhumation, based on: (1) the loss of Ni, Cr, V from the mantle, which is mirrored by a gain in the same elements in syn-kinematic minerals along rift-related extensional detachment faults, and (2) the enrichment of Si, Fe, Mn, Mg and other elements in the crust, and the overlying syn-hyperextension sedimentary rocks.

These observations are also confirmed by the mass change diagrams shown in Figures 7–9. Although the histograms show a wide range of element loss or gain, the method applied here must be seen as the probability of the loss/gain happening and provides a confidence interval for the occurrence of gain/loss. For instance, the example of Ni shows that losses can be between approximately -75% and 0% , considering the confidence interval for this element. Rather than look at this as an uncertainty, one should look at the probability that loss of Ni is occurring. The $P_{97.5}$ indicates that there is a 97.5% probability that Ni was lost during mantle alterations. It is worth to mention that the histogram distribution also encompasses all possible interactions between each protolith to altered rock interactions (i.e., between bootstrap samples), in this case between weakly altered peridotite (less than 10% of alteration) and serpentinites (between 10 to 95% of alteration). Therefore, if a peridotite is altered to 15%, the Ni loss will be much lower than if a peridotite is altered to 80%. The same rationale can be applied to the fault rocks over the continental crust showing a gain in Ni. The P_{50} of Ni points to an approximately 500% gain in Tasna and 100% gain in the Pyrenees and Iberia (Figure 8).

This leads to the question of where these elements come from and what processes are related to the release of these elements. Three potential sources exist for the elements observed as gain: a magmatic, a continental crustal, or a mantle source.

We exclude a magmatic source because, in the Iberia margin, the Late Aptian period is dominated by serpentinization rather than magmatic processes, as shown by drill hole data [49,86], refraction seismic data [24] and magnetic anomalies [23,31]. In the example of the Tasna OCT, mantle exhumation is not linked to magmatic activity. In the case of the Mauléon basin in the West Pyrenees, magmatism associated with mantle exhumation is extremely limited. Thus, the origin of the gained elements is difficult to explained through magmatic processes.

A crustal origin cannot be excluded for Si, Ca and other elements that are linked to the breakdown of feldspar, saussuritization and albitization reactions, which are all linked to Si-metasomatism. Thus, one cannot exclude the recycling of Si-rich continent-reacted fluids, as shown by Peverelli et al. [87]. In some cases, Si and Ca in fault rocks and tectono-sedimentary breccias are undoubtedly the product of early stages of water–rock reactions associated with the albitization/saussuritization of crustal rocks. In such examples [74], quartz and calcite veins are spatially and temporally linked to alterations within the host basement and altered feldspars are rimmed by quartz. However, in examples where the gains in Si and Ca are related to mantle-reacted fluids, centimetric quartz veins occur in the undeformed continental crust (i.e., outside the fault zone) associated with metals such as Cr, Ni and V, which are enriched relative to the continental host rock. Si-enrichment linked to mantle-reacted fluids is, therefore, best documented by the association with some trace (e.g., Ni, Cr and V) and major elements (e.g., Mg, Fe and Mn). However, more microstructural analyses, field relationship and diagenetic processes are needed to distinguish between the crustal and mantle origin of elements such as Si and Ca.

There are many studies on mass change during serpentinization [88–93]. Overall, there is only consensus about Ca mobility. For all the other elements, whether they can be mobilized during serpentinization is still debated. In our study, we document and quantify mass transfer between the mantle, the crust and sedimentary layers along detachment systems in hyperextended rift systems using well-documented examples that can be used to argue that the release of Mg, Fe, Si, Cr, Ni and V in the mantle causes enrichment in these and other elements in the adjacent crustal (fault) rocks and syn-tectonic sedimentary layers by using a Monte Carlo-based bootstrap approach to determine mass changes. This rather sophisticated approach circumvents some of the difficulties associated with more traditional approaches to quantifying mass transfer reactions in geological systems, which is a challenging problem. The results of our mass balance show that the loss of certain elements in the mantle (e.g., Ni, Cr and V) is mirrored by the enrichment of these elements in crustal fault rocks. This result is solid and supported by geological observations. However, this observation alone does not allow for us to define the processes that are at the origin of

the element transfer, and we cannot, at this stage, discriminate between the serpentinization and weathering of serpentinite or determine the redox conditions in the mantle-reacted fluids. Nevertheless, there are some clues from observations, laboratory experiments and geochemical modeling. For example, there is convincing and well-documented evidence for the weathering of serpentinite at the seafloor in the Iberian Margin [61]. Laboratory experiments (e.g., [94]) point out that the water–rock interaction between seawater and peridotite creates serpentine while the water is enriched in Ca, Si and Fe during the first stages of alteration and after it decreases, probably because the experiment was performed in a closed system. On the other hand, there is well-documented evidence from laboratory experiments and theoretical models that serpentinization retains Mg, Fe and Si, while Ca is largely lost [92,95–97]. Although most of these studies focused on MOR systems, these theoretical and experimental studies are likely also applicable to hyperextended systems at magma-poor margins. Thus, our observations of element transfer by mantle-reacted fluids seem to contradict some laboratory experiments. The fact that the transferred elements are within syn-kinematic minerals controlled by active detachment faults makes this process unlikely to be responsible for the observed element transfer. Thus, we consider that serpentinization during mantle exhumation in natural environments (not laboratory experiments) may be linked to element mobility. This assumption must be tested with experiments that are more comparable with natural analogs. Thus, this study provides fundamentally new insights into the serpentinization of ultramafic rocks associated with mantle exhumation at magma-poor rifted margins.

6.6. Model for Fluid Flow in Hyperextended Domains Linked to Mantle Exhumation

Based on the study of three examples of detachment faults from magma-poor, hyperextended domains, and by linking field observations with structural and geochemical analyses, we can demonstrate that mantle-reacted fluid circulation is not an exclusive process of a particular rift system, but is an intrinsic process associated with the evolution of magma-poor rifted margins summarized in Figure 11 and in Table 2.

At early stages of rifting and before detachment faults penetrate the mantle (Figure 11a), continental-crust-reacted fluids migrate along brittle fault zones and interact with the syn-tectonic sedimentary sequence (Figure 11a(a1)). When the crust is thinned to less than 10 km and fully embrittled, detachment faults can reach the mantle (Figure 11b(b1)). From this stage, seawater can infiltrate the mantle, starting with serpentinization. Subsequently, the mantle-reacted fluids migrate upwards along the active detachment faults affecting the pre- and syn-exhumation sediments (Figure 11c(c1); see also [4]). The coeval deposition of syn-mantle exhumation sediments “captured” the modified-seawater signature, as described for the Late Aptian sedimentary rocks from the Iberia margin. The element signature captured by sediments was also identified in syn-exhumation sedimentary rocks in the Alpine Tethyan margin [4].

In a subsequent stage, deformation is localized within the area of future breakup (Figure 11d(d1)) simultaneous with the onset of magma emplacement. In the next stage, mass transfer and hydrothermal activity ceased in the OCT and continued at the MOR (Figure 11e). During this stage, hydrothermal activity occurs far away from the OCT. It is important to mention that the thermal state, as well as the type of mantle involved in the hydration processes of OCT and MORs, are different.

Table 2. Major observations and insights from the studied sites.

Observations/Sites		Err and Platta System in the Alps [4]	West Pyrenees (Mauléon)	Alps (Tasna)	Iberia Margin (Hobby High)
Structural/ Microstructural and/or Field Observations of Fluid Circulation in OCT	Calcite veins with Fe-oxides in serpentinites	very common (see Figure 4d,e in Pinto et al. [4])	very common (e.g., Figure 6e).	very common (Figure 4(b1–b3)).	described on Site 1068 (Figure 5b(b1,b2)).
	Mineralization over exhumed mantle	centimetric Fe-oxides	centimetric Fe-oxides (Figure 6f)	not observed	described on Site 1068 (Figure 5b)
Field Observations of Fluid Circulation in OCT	Fault rocks: synkinematic phyllosilicates, extension related foliation and oxides	observed (see Figure 4d,e in Pinto et al. [4])	observed (Figure 6b,c)	observed along the UTD (Figure 4(a4))	described along the HHD (Figure 5(a2))
	Mineralization in the sedimentary rocks	hydrothermal cherts enriched in metals	Fe and Mn oxides at the fault break-away in the pre-rift sedimentary rocks (Figure 6g)	not investigated	not investigated
	Mass balance for serpentinised mantle rocks associated with detachment faulting	loss of major and minor/trace elements (e.g., Ca, Mg, Fe, Mn, Si, Ni, Cr and V)	not investigated	not investigated	not investigated
Geochemistry	Mass balance for continental crust associated with detachment faulting	gain of metals (eg., Ni, Cr, V) gain of these metals not observed in faults that are in a more proximal position in the margin	gain in metals (e.g., Ni, Cr, V) in fault rocks comparing to host rock protoliths	gain in metals (e.g., Ni, Cr, V) in fault rocks when compared to the protolith in the footwall	gain of metals (eg., Ni, Cr, V) in fault rocks
	Supra-detachment sedimentary sequence	metal concentration increases toward the top of the syn-rift sedimentary sequence and is maximal in the sequence that is deposited during mantle exhumation (see their Figure 11). gradual decrease of these metal in post-exhumation sedimentary sequences (see Figure 11 in Pinto et al. [4])	not investigated	not investigated	external source of Si (high temperature) Si, Mg and Mn increases in the syn-exhumation/serpentinization sedimentary sequence (Figure 10)
Major insight from each site		<ul style="list-style-type: none"> mass balance showing that metal lost in the mantle are the same gained along Err Detachment system resulted from mantle-reacted fluids syn-rift sedimentary sequence over thinned continental crust records interaction with mantle-reacted fluids (see Figures 16 and 17 in Pinto et al. [4]) 	mantle-reacted fluid circulation along Albian to Cenomanian extensional detachment fault in the continental crust (NMD)	gain of mantle-derived elements in fault rocks show that circulation of mantle-reacted fluids in the continental crust was an important process during OCT formation	in addition to field and petrological evidence, this site is important to compare results with rifts preserved in orogens. The results show that fluids along faults are rift-related and not associated with orogenesis. They also support the idea that fluids are a characteristic element that needs to be considered in the evolution of magma-poor rifted margins.

7. Conclusions

Evidence for deep fluid flow at the Iberia distal margin, in the hyperextended Mauléon Basin in the Pyrenees and the Tasna OCT belonging to the Alpine Tethys, shows that fluid flow is an important geological process to explain element transfer and is intimately linked to hyperextension at the most distal parts of magma-poor rifted margins. In hyperextended systems, two distinctive types of fluids are documented: continental-crust-reacted fluids and mantle-reacted fluids. The first one is the consequence of the saussuritization that occurs during detachment fault activity in the continental crust, and the second one is related to the alterations in mantle rocks triggered by faults cutting through the thinned continental crust and rooting in the mantle. The composition of continental-crust-reacted fluids is best depicted by Ca and Si, which can be observed through their imprints along extensional detachment faults and the overlying tectono-sedimentary breccias. The mantle-reacted fluids are best characterized by gains in Si, Ca, Mg, Fe, Mn, Ni, Cr and V. Their imprint can also be recorded along extensional detachment systems and within pre- to syn-exhumation sedimentary rocks. As the observed Si in Aptian sedimentary rocks from the Iberia Margin is accompanied by mantle-derived metals and is tectonically linked to the age of exhumation, we attributed these to mantle-reacted fluids rather than continental-reacted fluids.

The evolution of hyperextended domains is coeval to the formation of restricted basins that are not fully connected to the open global ocean. Therefore, the observed fluid flow and element transfer may have an impact on the marine waters and diagenetic processes, affecting hyperextended basins. As the fluid flow also results in the hydration of both continental crust and mantle rocks, it changes the rheology and may impact the thermal evolution of hyperextended systems. The results of this study may also have important implications for ore mineral exploration in hyperextended rift systems. As the mantle-reacted fluids are observed in syn-exhumation sedimentary rocks, the geochemical analyses, together with tectono-stratigraphic studies, may be used as a proxy for understanding the time and duration of mantle exhumation and alteration and the first sedimentary processes in present-day magma-poor rifted margins.

Supplementary Materials: The following supporting information can be downloaded at: <https://www.mdpi.com/article/10.3390/geosciences13120374/s1>, “Gain and Losses of Elements Calculations”.

Author Contributions: Conceptualization, V.H.G.P.; Methodology, V.H.G.P., A.M.K., R.A.V. and M.U.; Software, V.H.G.P. and R.A.V.; Validation, V.H.G.P. and G.M.; Formal analysis, V.H.G.P. and A.M.K.; Investigation, V.H.G.P. and E.M.; Resources, G.M. and A.R.V.; Writing—original draft, V.H.G.P.; Writing—review & editing, V.H.G.P., G.M., A.M.K. and A.R.V.; Visualization, V.H.G.P.; Supervision, G.M. and E.M.; Funding acquisition, A.R.V. All authors have read and agreed to the published version of the manuscript.

Funding: This research was funded by Petrobras S.A. and developed at the University of Strasbourg and CNRS facilities.

Data Availability Statement: Some of the serpentinized peridotite data are from Müntener et al. [70] and Pinto et al. [4]. The fault rock data from the Hobby High are from Whitmarsh et al. [46].

Acknowledgments: We are thankful to Nick Hayman, Catriona Menzies, Francesca Piccoli, Frieder Klein and anonymous reviewers for very constructive reviews and valuable comments that allowed us to improve the manuscript. We are grateful to the editorial team, specially Assistant Editor for handling the manuscript.

Conflicts of Interest: The funders had no role in the design of the study; in the collection, analyses, or interpretation of data; in the writing of the manuscript; or in the decision to publish the results.

References

1. Reynolds, S.J.; Lister, G.S. Structural aspects of fluid-rock interactions in detachment zones. *Geology* **1987**, *15*, 362–366. [[CrossRef](#)]
2. Hayman, N.W. Shallow crustal fault rocks from the Black Mountain detachments, Death Valley, CA. *J. Struct. Geol.* **2006**, *28*, 1767–1784. [[CrossRef](#)]

3. McCaig, A.M.; Cliff, R.A.; Escartin, J.; Fallick, A.E.; MacLeod, C.J. Oceanic detachment faults focus very large volumes of black smoker fluids. *Geology* **2007**, *35*, 935. [[CrossRef](#)]
4. Pinto, V.H.G.; Manatschal, G.; Karpoff, A.M.; Viana, A. Tracing mantle-reacted fluids in magma-poor rifted margins: The example of Alpine Tethyan rifted margins. *Geochem. Geophys. Geosyst.* **2015**, *16*, 3271–3308. [[CrossRef](#)]
5. Corre, B.; Boulvais, P.; Boiron, M.C.; Lagabrielle, Y.; Marasi, L.; Clerc, C. Fluid circulations in response to mantle exhumation at the passive margin setting in the north Pyrenean zone, France. *Mineral. Petrol.* **2018**, *112*, 647–670. [[CrossRef](#)]
6. Cruset, D.; Vergés, J.; Muñoz-López, D.; Moragas, M.; Cantarero, I.; Travé, A. Fluid evolution from extension to compression in the Pyrenean Fold Belt and Basque-Cantabrian Basin: A review. *Earth-Sci. Rev.* **2023**, *243*, 104494. [[CrossRef](#)]
7. Bach, W.; Jöns, N.; Klein, F. Metasomatism within the ocean crust. In *Metasomatism and the Chemical Transformation of Rock: The Role of Fluids in Terrestrial and Extraterrestrial Processes*; Springer: Berlin/Heidelberg, Germany, 2013; pp. 253–288. [[CrossRef](#)]
8. Boschi, C.; Früh-Green, G.L.; Delacour, A.; Karson, J.A.; Kelley, D.S. Mass transfer and fluid flow during detachment faulting and development of an oceanic core complex, Atlantis Massif (MAR 30 °N). *Geochem. Geophys. Geosyst.* **2006**, *7*, 1–39. [[CrossRef](#)]
9. Schwarzenbach, E.M.; Früh-Green, G.L.; Bernasconi, S.M.; Alt, J.C.; Plas, A. Serpentinization and carbon sequestration: A study of two ancient peridotite-hosted hydrothermal systems. *Chem. Geol.* **2013**, *351*, 115–133. [[CrossRef](#)]
10. Castelain, T.; McCaig, A.M.; Cliff, R.A. Fluid evolution in an Oceanic Core Complex: A fluid inclusion study from IODP hole U1309 D-Atlantis Massif, 30 °N, Mid-Atlantic Ridge. *Geochem. Geophys. Geosyst.* **2014**, *15*, 1193–1214. [[CrossRef](#)]
11. Seyfried, W.E.; Pester, N.J.; Tutolo, B.M.; Ding, K. The Lost City hydrothermal system: Constraints imposed by vent fluid chemistry and reaction path models on seafloor heat and mass transfer processes. *Geochim. Cosmochim. Acta* **2015**, *163*, 59–79. [[CrossRef](#)]
12. Humphris, S.E.; Klein, F. Progress in Deciphering the Controls on the Geochemistry of Fluids in Seafloor Hydrothermal Systems. *Annu. Rev. Mar. Sci.* **2018**, *10*, 315–343. [[CrossRef](#)] [[PubMed](#)]
13. Kelley, D.S.; Karson, J.A.; Blackman, D.K.; Früh-Green, G.L.; Butterfield, D.A.; Lilley, M.D.; Olson, E.J.; Schrenk, M.O.; Roe, K.K.; Lebon, G.T.; et al. An off-axis hydrothermal vent field near the Mid-Atlantic Ridge at 30 degrees N. *Nature* **2001**, *412*, 145–149. [[CrossRef](#)] [[PubMed](#)]
14. Shanks, W.C. Stable isotopes in seafloor hydrothermal systems: Vent fluids, hydrothermal deposits, hydrothermal alteration, and microbial processes. *Rev. Mineral. Geochem.* **2001**, *43*, 469–525. [[CrossRef](#)]
15. Fouquet, Y.; Cambon, P.; Etoubleau, J.; Charlou, J.L.; Ondréas, H.; Barriga, F.J.; Cherkashov, G.; Semkova, T.; Poroshina, I.; Bohn, M.; et al. Geodiversity of hydrothermal processes along the Mid-Atlantic Ridge and ultramafic-hosted mineralization: A new type of oceanic Cu-Zn-Co-Au volcanogenic massive sulfide deposit. In *Diversity of Hydrothermal Systems on Slow Spreading Ocean Ridges*; AGU: Washington, DC, USA, 2010; Volume 188, pp. 321–367.
16. Coltat, R.; Boulvais, P.; Branquet, Y.; Collot, J.; Epin, M.E.; Manatschal, G. Syntectonic carbonation during synmagmatic mantle exhumation at an ocean-continent transition. *Geology* **2019**, *47*, 183–186. [[CrossRef](#)]
17. Dias, Á.S.; Barriga, F.J.A.S. Mineralogy and geochemistry of hydrothermal sediments from the serpentinite-hosted Saldanha hydrothermal field (36°34' N; 33°26' W) at MAR. *Mar. Geol.* **2006**, *225*, 157–175. [[CrossRef](#)]
18. Dias, Á.S.; Früh-Green, G.L.; Bernasconi, S.M.; Barriga, F.J.A.S. Geochemistry and stable isotope constraints on high-temperature activity from sediment cores of the Saldanha hydrothermal field. *Mar. Geol.* **2011**, *279*, 128–140. [[CrossRef](#)]
19. Incerpi, N.; Martire, L.; Manatschal, G.; Bernasconi, S.M.; Gerdes, A.; Czuppon, G.; Palcsu, L.; Karner, G.D.; Johnson, C.A.; Figueredo, P.H. Hydrothermal fluid flow associated to the extensional evolution of the Adriatic rifted margin: Insights from the pre- to post-rift sedimentary sequence (SE Switzerland, N ITALY). *Basin Res.* **2020**, *32*, 91–115. [[CrossRef](#)]
20. Manatschal, G. Fluid-and reaction-assisted low-angle normal faulting: Evidence from rift-related brittle fault rocks in the Alps (Err Nappe, eastern Switzerland). *J. Struct. Geol.* **1999**, *21*, 777–793. [[CrossRef](#)]
21. Nteme Mukonzo, J.; Boiron, M.-C.; Lagabrielle, Y.; Cathelineau, M.; Quesnel, B. Fluid–rock interactions along detachment faults during continental rifting and mantle exhumation: The case of the Urdach Iherzolite body (North Pyrenees). *J. Geol. Soc.* **2021**, *178*, jgs2020-116. [[CrossRef](#)]
22. Boillot, G.; Girardeau, J.; Kornprobst, J. 41. Rifting of the Galicia Margin: Crustal thinning and emplacement of mantle rocks on the seafloor. In *Proceedings of the Ocean Drilling Program, Scientific Results*; Boillot, G., Winterer, E.L., Meyer, A.W., Applegate, M.B., Baltuck, M., Bergen, J.A., Comas, M.C., Davies, T.A., Dunham, K., Evans, C.A., et al., Eds.; Ocean Drilling Program: College Station, TX, USA, 1988; Volume 103, pp. 741–756. [[CrossRef](#)]
23. Minshull, T.A.; Dean, S.M.; Whitmarsh, R.B. The peridotite ridge province in the Southern Iberia Abyssal Plain: Seismic constraints revisited. *J. Geophys. Res. Solid Earth* **2014**, *119*, 1580–1598. [[CrossRef](#)]
24. Dean, S.M.; Minshull, T.A.; Whitmarsh, R.B.; Loudon, K.E. Deep structure of the ocean-continent transition in the southern Iberia Abyssal Plain from seismic refraction profiles: The IAM-9 transect at 40°20'N. *J. Geophys. Res. Solid Earth* **2000**, *105*, 5859–5885. [[CrossRef](#)]
25. Pinto, V.H.G.; Manatschal, G.; Karpoff, A.M.; Ulrich, M.; Viana, A.R. Seawater storage and element transfer associated with mantle serpentinization in magma-poor rifted margins: A quantitative approach. *Earth Planet. Sci. Lett.* **2017**, *459*, 227–237. [[CrossRef](#)]
26. Incerpi, N.; Manatschal, G.; Martire, L.; Bernasconi, S.M.; Gerdes, A.; Bertok, C. Characteristics and timing of hydrothermal fluid circulation in the fossil Pyrenean hyperextended rift system: New constraints from the Chainons Béarnais (W Pyrenees). *Int. J. Earth Sci.* **2020**, *109*, 1071–1093. [[CrossRef](#)]

27. Tucholke, B.; Sibuet, J.C. Problematic plate reconstruction. *Nature Geosci.* **2012**, *5*, 676–677. [[CrossRef](#)]
28. Manatschal, G.; Müntener, O. A type sequence across an ancient magma-poor ocean–continent transition: The example of the western Alpine Tethys ophiolites. *Tectonophysics* **2009**, *473*, 4–19. [[CrossRef](#)]
29. Sutra, E.; Manatschal, G.; Mohn, G.; Unternehr, P. Quantification and restoration of extensional deformation along the Western Iberia and Newfoundland rifted margins. *Geochem. Geophys. Geosyst.* **2013**, *14*, 2575–2597. [[CrossRef](#)]
30. Nirrengarten, M.; Manatschal, G.; Yuan, X.P.; Kuszniir, N.J.; Maillot, B. Application of the critical Coulomb wedge theory to hyper-extended, magma-poor rifted margins. *Earth Planet. Sci. Lett.* **2016**, *442*, 121–132. [[CrossRef](#)]
31. Bronner, A.; Sauter, D.; Manatschal, G.; Péron-Pinvidic, G.; Munsch, M. Magmatic breakup as an explanation for magnetic anomalies at magma-poor rifted margins. *Nat. Geosci.* **2011**, *4*, 549–553. [[CrossRef](#)]
32. Manatschal, G.; Sauter, D.; Karpoff, A.M.; Masini, E.; Mohn, G.; Lagabrielle, Y. The Chenaillet Ophiolite in the French/Italian Alps: An ancient analogue for an Oceanic Core Complex? *Lithos* **2011**, *124*, 169–184. [[CrossRef](#)]
33. Beltrando, M.; Manatschal, G.; Mohn, G.; Dal Piaz, G.V.; Vitale Brovarone, A.; Masini, E. Recognizing remnants of magma-poor rifted margins in high-pressure orogenic belts: The Alpine case study. *Earth-Sci. Rev.* **2014**, *131*, 88–115. [[CrossRef](#)]
34. Ribes, C.; Petri, B.; Ghienne, J.F.; Manatschal, G.; Galster, F.; Karner, G.D.; Figueredo, P.H.; Johnson, C.A.; Karpoff, A.M. Tectono-sedimentary evolution of a fossil ocean-continent transition: Tasna nappe, central Alps (SE Switzerland). *Bull. Geol. Soc. Am.* **2020**, *132*, 1427–1446. [[CrossRef](#)]
35. Picazo, S.; Manatschal, G.; Cannat, M.; Andréani, M. Deformation associated to exhumation of serpentized mantle rocks in a fossil Ocean Continent Transition: The Totalp unit in SE Switzerland. *Lithos* **2013**, *175*, 255–271. [[CrossRef](#)]
36. Masini, E.; Manatschal, G.; Tugend, J.; Mohn, G.; Flament, J.-M. The tectono-sedimentary evolution of a hyperextended rift basin: The example of the Arzac–Mauléon rift system (Western Pyrenees, SW France). *Int. J. Earth Sci.* **2014**, *103*, 1569–1596. [[CrossRef](#)]
37. Saspiturry, N.; Issautier, B.; Razin, P.; Baudin, T.; Asti, R.; Lagabrielle, Y.; Allanic, C.; Serrano, O.; Duretz, T. Review of Iberia–Eurasia Plate-Boundary Basins: Role of Sedimentary Burial and Salt Tectonics during Rifting and Continental Breakup. *Basin Research* **2021**, *33*, 1626–1661. [[CrossRef](#)]
38. Hochscheid, F.; Coltat, R.; Ulrich, M.; Munoz, M.; Manatschal, G.; Boulvais, P. The Sr isotope geochemistry of oceanic ultramafic-hosted mineralizations. *Ore Geol. Rev.* **2022**, *144*, 104824. [[CrossRef](#)]
39. Florineth, D.; Froitzheim, N. Transition from continental to oceanic basement in the Tasna nappe (Engadine window, Graubünden, Switzerland): Evidence for Early Cretaceous opening of the Valais ocean. *Schweiz. Mineral. Petrogr. Mitteilungen* **1994**, *74*, 437–448.
40. Manatschal, G.; Engström, A.; Desmurs, L.; Schaltegger, U.; Cosca, M.; Müntener, O.; Bernoulli, D. What is the tectono-metamorphic evolution of continental break-up: The example of the Tasna Ocean–Continent Transition. *J. Struct. Geol.* **2006**, *28*, 1849–1869. [[CrossRef](#)]
41. Masini, E.; Manatschal, G.; Mohn, G.; Ghienne, J.-F.; Lafont, F. The tectono-sedimentary evolution of a supra-detachment rift basin at a deep-water magma-poor rifted margin: The example of the Samedan Basin preserved in the Err nappe in SE Switzerland. *Basin Res.* **2011**, *23*, 652–677. [[CrossRef](#)]
42. Evans, B.W.; Hattori, K.; Baronnet, A. Serpentine: What, Why, Where? *Elements* **2013**, *9*, 99–106. [[CrossRef](#)]
43. Hauser, A.-C.; Müntener, O. New age constraints on the opening of the Piemonte-Ligurian Ocean (Tasna-Nauders area, CH-A). In Proceedings of the 9th Swiss Geoscience Meeting, Zurich, Switzerland, 11–13 November 2011.
44. Li, X.-H.; Faure, M.; Lin, W.; Manatschal, G. New isotopic constraints on age and magma genesis of an embryonic oceanic crust: The Chenaillet Ophiolite in the Western Alps. *Lithos* **2013**, *160*, 283–291. [[CrossRef](#)]
45. Sawyer, D.S.; Whitmarsh, R.B.; Klaus, A.; Beslier, M.O.; Collins, E.S.; Comas, M.C.; Cornen, G.; Kaenel, E.; Pinheiro, L.M.; Gervais, E.; et al. *Proceedings of the Ocean Drilling Program, Initial Reports*, 149; Ocean Drilling Program: College Station, TX, USA, 1994; p. 268. [[CrossRef](#)]
46. Whitmarsh, R.B.; Beslier, M.O.; Wallace, P.J. *Proceedings of the Ocean Drilling Program, Initial Reports*, 173; Ocean Drilling Program: College Station, TX, USA, 1998.
47. Manatschal, G.; Froitzheim, N.; Rubenach, M.; Turrin, B.D. The role of detachment faulting in the formation of an ocean-continent transition: Insights from the Iberia Abyssal Plain. *Geol. Soc. Lond. Spec. Publ.* **2001**, *187*, 405–428. [[CrossRef](#)]
48. Wilson, R.C.L.; Manatschal, G.; Wise, S. Rifting along non-volcanic passive margins: Stratigraphic and seismic evidence from the Mesozoic successions of the Alps and Western Iberia. *Geol. Soc. Lond. Spec. Publ.* **2001**, *187*, 429–452. [[CrossRef](#)]
49. Jagoutz, O.; Müntener, O.; Manatschal, G.; Rubatto, D.; Péron-Pinvidic, G.; Turrin, B.D.; Villa, I.M. The rift-to-drift transition in the North Atlantic: A stuttering start of the MORB machine? *Geology* **2007**, *35*, 1087. [[CrossRef](#)]
50. Jammes, S.; Manatschal, G.; Lavier, L.; Masini, E. Tectonosedimentary evolution related to extreme crustal thinning ahead of a propagating ocean: Example of the western Pyrenees. *Tectonics* **2009**, *28*, 4. [[CrossRef](#)]
51. Fortane, A.; Duee, G.; Lagabrielle, Y.; Coutelle, A. Lherzolites and the western “Chainons bernois” (French Pyrenees): Structural and paleogeographical pattern. *Tectonophysics* **1986**, *129*, 81–98. [[CrossRef](#)]
52. Lagabrielle, Y.; Bodinier, J.L. Submarine reworking of exhumed subcontinental mantle rocks: Field evidence from the Lherz peridotites, French Pyrenees. *Terra Nova* **2008**, *20*, 11–21. [[CrossRef](#)]
53. Lagabrielle, Y.; Labaume, P.; de Saint Blanquat, M. Mantle exhumation, crustal denudation, and gravity tectonics during Cretaceous rifting in the Pyrenean realm (SW Europe): Insights from the geological setting of the Lherzolite bodies. *Tectonics* **2010**, *29*, TC4012. [[CrossRef](#)]

54. Cadenas, P.; Lescoutre, R.; Manatschal, G.; Fernández-Viejo, G. The role of extensional detachment systems in thinning the crust and exhuming granulites: Analogies between the offshore le Danois High and the onshore Labourd Massif in the Biscay/Pyrenean rifts. *BSGF-Earth Sci. Bull.* **2021**, *192*, 57. [[CrossRef](#)]
55. Hart, N.R.; Stockli, D.F.; Lavier, L.L.; Hayman, N.W. Thermal evolution of a hyperextended rift basin, Mauléon Basin, western Pyrenees. *Tectonics* **2017**, *36*, 1103–1128. [[CrossRef](#)]
56. Hébert, R.; Beaudoin, G.; Rochon, M.; Gardien, V. Metamorphic evolution and oxygen isotope geochemistry of rift-precursor amphibolites from Hole 1067A ODP Leg 173 off West Iberian Galicia Bank rifted margin. *Lithos* **2008**, *101*, 162–176. [[CrossRef](#)]
57. Boissonnas, J.; Destombes, J.; Heddebaut, C.; Le Pochat, G.; Lorisgnol, S.; Roger, P.; Ternet, Y. *Carte Géologique de France au 1/50,000*; Chapter Feuille de Iholdy; BRGM: Orléans, France, 1964.
58. Moody, J.B. Serpentinization: A review. *Lithos* **1976**, *9*, 125–138. [[CrossRef](#)]
59. Früh-Green, G.L.; Weissert, H.; Bernoulli, D. A multiple fluid history recorded in Alpine ophiolites. *J. Geol. Soc. Lond.* **1990**, *147*, 959–970. [[CrossRef](#)]
60. Evans, C.A.; Baltuck, M. 15. Low-temperature alteration of peridotite, Hole 637A. In *Proceedings of the Ocean Drilling Program, Scientific Results*; Ocean Drilling Program: College Station, TX, USA, 1988; Volume 103, pp. 235–239.
61. Milliken, K.; Morgan, J. Chemical evidence for near-seafloor precipitation of calcite in serpentinites (Site 897) and serpentinite breccias (Site 899). Iberia abyssal plain. In *Proceedings of the Ocean Drilling Program, Scientific Results*; Whitmarsh, R.B., Sawyer, D.S., Klaus, D.G., Masson, A., Eds.; Ocean Drilling Program: College Station, TX, USA, 1996; Volume 149, pp. 553–558.
62. Skelton, A.D.; Valley, J.W. The relative timing of serpentinisation and mantle exhumation at the ocean–continent transition, Iberia: Constraints from oxygen isotopes. *Earth Planet. Sci. Lett.* **2000**, *178*, 327–338. [[CrossRef](#)]
63. Engström, A.; Skelton, A.; Grassineau, N. Isotopic and petrological evidence of fluid–rock interaction at a Tethyan ocean–continent transition in the Alps: Implications for tectonic processes and carbon transfer during early ocean formation. *Geofluids* **2007**, *7*, 401–414. [[CrossRef](#)]
64. Clerc, C.; Boulvais, P.; Lagabrielle, Y.; de Saint Blanquat, M. Ophicalcites from the northern Pyrenean belt: A field, petrographic and stable isotope study. *Int. J. Earth Sci.* **2013**, *103*, 141–163. [[CrossRef](#)]
65. DeFelipe, I.; Pedreira, D.; Pulgar, J.A.; Iriarte, E.; Mendia, M. Mantle exhumation and metamorphism in the Basque-Cantabrian Basin (N Spain): Stable and clumped isotope analysis in carbonates and comparison with ophicalcites in the North-Pyrenean Zone (Urdach and Lherz). *Geochem. Geophys. Geosyst.* **2017**, *18*, 631–652. [[CrossRef](#)]
66. Beard, J.S.; Hopkinson, L. A fossil, serpentinization-related hydrothermal vent, Ocean Drilling Program Leg 173, Site 1068 (Iberia Abyssal Plain): Some aspects of mineral and fluid chemistry. *J. Geophys. Res.* **2000**, *105*, 16527. [[CrossRef](#)]
67. Morgan, J.K.; Milliken, K.L. Petrography of calcite veins in serpentinized peridotite basement rocks from the Iberia abyssal plain, Sites 897 and 899: Kinematic and environmental implications. In *Proceedings of the Ocean Drilling Program, Scientific Results*; Whitmarsh, R.B., Sawyer, D.S., Klaus, A., Masson, D.G., Eds.; Ocean Drilling Program: College Station, TX, USA, 1996; Volume 149, pp. 559–569.
68. Boillot, G.; Winterer, E.L.; Meyer, A.W. (Eds.) Introduction, objectives, and principal results: Ocean Drilling Program Leg 103, West Galicia Margin. In *Proceedings of the Ocean Drilling Program, 103 Initial Reports*; Ocean Drilling Program: College Station, TX, USA, 1987.
69. Govindaraju, K. 1995 working values with confidence limits for twenty-six CRPG, ANRT and IWG-GIT geostandards. *Geostand. Newsl.* **1995**, *19*, 1–32. [[CrossRef](#)]
70. Müntener, O.; Manatschal, G.; Desmurs, L.; Pettke, T. Plagioclase Peridotites in Ocean–Continent Transitions: Refertilized Mantle Domains Generated by Melt Stagnation in the Shallow Mantle Lithosphere. *J. Petrol.* **2010**, *51*, 255–294. [[CrossRef](#)]
71. Clauser, S.; Renard, M.; Richebois, G. 29. Variations in trace element contents and isotopic compositions of lower cretaceous carbonates from the Galicia Margin (ODP, Leg 103): Reconstruction of the paleochemistry of the early Cretaceous Ocean. In *Proceedings of the Ocean Drilling Program, Scientific Results*; Ocean Drilling Program: College Station, TX, USA, 1988; Volume 103, pp. 115–117.
72. Ague, J.J.; Van Haren, J.L.M. Assessing metasomatic mass and volume changes using the bootstrap, with application to deep crustal hydrothermal alteration of marble. *Econ. Geol.* **1996**, *91*, 1169–1182. [[CrossRef](#)]
73. MacLean, W.H.; Barrett, T.J. Lithochemical techniques using immobile elements. *J. Geochem. Explor.* **1993**, *48*, 109–133. [[CrossRef](#)]
74. Manatschal, G.; Marquer, D.; Früh-Green, G.L. Channelized fluid flow and mass transfer along a rift-related detachment fault (Eastern Alps, southeast Switzerland). *Geol. Soc. Am. Bull.* **2000**, *112*, 21. [[CrossRef](#)]
75. Hébert, R.; Gueddari, K.; LaFleche, M.R.; Beslier, M.-O.; Gardien, V. Petrology and geochemistry of exhumed peridotites and gabbros at non-volcanic margins: ODP Leg 173 West Iberia ocean–continent transition zone. *Geol. Soc. Lond. Spec. Publ.* **2001**, *187*, 161–189. [[CrossRef](#)]
76. Fabriès, J.; Lorand, J.-P.; Bodinier, J.-L. Petrogenetic evolution of orogenic lherzolite massifs in the central and western Pyrenees. *Tectonophysics* **1998**, *292*, 145–167. [[CrossRef](#)]
77. Baker, P.A.; Gieskes, J.M.; Elderfield, H. Diagenesis of Carbonates in Deep-Sea Sediments—Evidence From SR/CA Ratios and Interstitial Dissolved SR²⁺ Data. *SEPM J. Sediment. Res.* **1982**, *52*, 71–82. [[CrossRef](#)]
78. Graham, D.W.; Bender, M.L.; Williams, D.F.; Keigwin, L.D. Strontium–calcium ratios in Cenozoic planktonic foraminifera. *Geochim. Cosmochim. Acta* **1982**, *46*, 1281–1292. [[CrossRef](#)]

79. Ando, A.; Kawahata, H.; Kakegawa, T. Sr/Ca ratios as indicators of varying modes of pelagic carbonate diagenesis in the ooze, chalk and limestone realms. *Sediment. Geol.* **2006**, *191*, 37–53. [[CrossRef](#)]
80. Meyer, A.W.; Davies, T.A. Clay mineralogy of sediments from the Galicia Margin, ODP Leg 103. In *Proceedings of the Ocean Drilling Program Scientific Results, 103*; Boillot, G., Winterer, E.L., Meyer, A.W., Applegate, M.B., Baltuck, M., Bergen, J.A., Comas, M.C., Davies, T.A., Dunham, K., Evans, C.A., et al., Eds.; Ocean Drilling Program: College Station, TX, USA, 1988; pp. 461–475. [[CrossRef](#)]
81. Haggerty, J.A.; Germann, S.H. Resedimentation and diagenesis, including silicification, of barremian-aptian shallow-water carbonates from the Galicia Margin, Eastern North Atlantic, at ocean drilling program site 641. In *Proceedings of the Ocean Drilling Program, Scientific Results 103*; Boillot, G., Winterer, E.L., Meyer, A.W., Applegate, J., Eds.; Ocean Drilling Program: College Station, TX, USA, 1988; Volume 103, pp. 513–530.
82. Perseil, E.A.; Latouche, L. Découverte de microstructures de nodules polymétalliques dans les minéralisations manganésifères métamorphiques de Falotta et de Parsetens (Grisons-Suisse). *Miner. Depos.* **1989**, *24*, 111–116. [[CrossRef](#)]
83. Coltat, R.; Boulvais, P.; Riegler, T.; Pelleter, E.; Branquet, Y. Element Distribution in the Root Zone of Ultramafic-Hosted Black Smoker-like Systems: Constraints from an Alpine Analog. *Chem. Geol.* **2021**, *559*, 119916. [[CrossRef](#)]
84. McKenzie, J.A.; Isern, A.; Karpoff, A.M.; Swart, P.K. Basal dolomitic sediments, Tyrrhenian sea, ocean drilling program leg 107. In *Proceedings of the Ocean Drilling Program, 107 Scientific Results*; Kastens, K.A., Mascle, J., Auroux, C., Bonatti, E., Broglia, C., Channel, J., Curzi, P., Emeis, K.C., Glaçon, G., Hasegawa, S., et al., Eds.; Ocean Drilling Program: College Station, TX, USA, 1990; Volume 107, pp. 141–152.
85. Péron-Pinvidic, G.; Manatschal, G.; Minshull, T.; Sawyer, D. Tectonosedimentary Evolution of the Deep Iberia-Newfoundland Margins: Evidence for a Complex Breakup History. *Tectonics* **2007**, *26*, TC2011. [[CrossRef](#)]
86. Shipboard Scientific Party. Leg 210 summary. In *Ocean Drilling Program Leg 210*; Tucholke, B.E., Sibuet, J.-C., Klaus, A., Eds.; Ocean Drilling Program: College Station, TX, USA, 2004; Volume 210, pp. 1–78.
87. Peverelli, V.; Berger, A.; Wille, M.; Pettke, T.; Lanari, P.; Villa, I.M.; Herwegh, M. Epidote dissolution–precipitation during viscous granular flow: A micro-chemical and isotope study. *EGU Sphere* **2022**, *2022*, 1–29. [[CrossRef](#)]
88. Boschi, C.; Dini, A.; Früh-Green, G.L.; Kelley, D.S. Isotopic and element exchange during serpentinization and metasomatism at the Atlantis Massif (MAR 30 °N): Insights from B and Sr isotope data. *Geochim. Cosmochim. Acta* **2008**, *72*, 1801–1823. [[CrossRef](#)]
89. Harvey, J.; Savov, I.P.; Agostini, S.; Cliff, R.A.; Walshaw, R. Si-metasomatism in serpentinized peridotite: The effects of talc-alteration on strontium and boron isotopes in abyssal serpentinites from Hole 1268a, ODP Leg 209. *Geochim. Cosmochim. Acta* **2014**, *126*, 30–48. [[CrossRef](#)]
90. Malvoisin, B. Mass transfer in the oceanic lithosphere: Serpentinization is not isochemical. *Earth Planet. Sci. Lett.* **2015**, *430*, 75–85. [[CrossRef](#)]
91. Roumejon, S.; Cannat, M.; Agrinier, P.; Godard, M.; Andreani, M. Serpentinization and Fluid Pathways in Tectonically Exhumed Peridotites from the Southwest Indian Ridge (62–65 E). *J. Petrol.* **2015**, *56*, 703–734. [[CrossRef](#)]
92. Klein, F.; Le Roux, V. Quantifying the volume increase and chemical exchange during serpentinization. *Geology* **2020**, *48*, 552–556. [[CrossRef](#)]
93. de Obeso, J.C.; Kelemen, P.B. Major element mobility during serpentinization, oxidation and weathering of mantle peridotite at low temperatures. *Philos. Trans. R. Soc. A Math. Phys. Eng. Sci.* **2020**, *378*, 20180433. [[CrossRef](#)]
94. Seyfried, W.E.J.; Foustoukos, D.I.; Fu, Q. Redox evolution and mass transfer during serpentinization: An experimental and theoretical study at 200 °C, 500 bar with implications for ultramafic-hosted hydrothermal systems at Mid-Ocean Ridges. *Geochim. Cosmochim. Acta* **2007**, *71*, 3872–3886. [[CrossRef](#)]
95. Wetzel, L.R.; Shock, E.L. Distinguishing ultramafic-from basalt-hosted submarine hydrothermal systems by comparing calculated vent fluid compositions. *J. Geophys. Res. Solid Earth* **2000**, *105*, 8319–8340. [[CrossRef](#)]
96. Palandri, J.L.; Reed, M.H. Geochemical models of metasomatism in ultramafic systems: Serpentinization, rodingitization, and sea floor carbonate chimney precipitation. *Geochim. Cosmochim. Acta* **2004**, *68*, 1115–1133. [[CrossRef](#)]
97. Frost, R.B.; Beard, J.S. On silica activity and serpentinization. *J. Petrol.* **2007**, *48*, 1351–1368. [[CrossRef](#)]

Disclaimer/Publisher’s Note: The statements, opinions and data contained in all publications are solely those of the individual author(s) and contributor(s) and not of MDPI and/or the editor(s). MDPI and/or the editor(s) disclaim responsibility for any injury to people or property resulting from any ideas, methods, instructions or products referred to in the content.